RSC Advances

PAPER

View Article Online
View Journal | View Issue

Cite this: *RSC Adv.*, 2026, **16**, 10904

Synergistic radical scavenging effect of $NiSe_2$-doped SnO_2 nanocomposites: role of oxygen vacancies revealed by post-reaction characterizations

Mohamed Ashik Syra, Sangeetha Alaguvel and Devikala Sundaramurthy*

Received 7th January 2026
Accepted 4th February 2026

DOI: 10.1039/d6ra00150e

rsc.li/rsc-advances

Antioxidant imbalance plays a major role in triggering inflammation, cellular damage, and the progression of chronic diseases. Conventional antioxidants are limited by rapid degradation, poor stability, and low radical scavenging efficiency, creating the need for sustainable materials with improved antioxidant properties. Designing such materials requires a precise understanding on the fundamental radical scavenging mechanisms, particularly how electron transfer, surface defects and reactive active sites contribute to efficient radical neutralization for light-free scavenging. In this work, undoped and $NiSe_2$-doped SnO_2 nanocomposites (10%, 20% and 30%) were synthesised and evaluated for antibacterial and antioxidant activity using the DPPH assay (light-free scavenging). XRD, UV-vis spectroscopy, FTIR spectroscopy, HRSEM, HRTEM, FESEM, ESR, and XPS techniques were used to confirm the formation of nanocomposites and to characterise their structural and physicochemical properties. XRD peak shifts confirmed the successful incorporation of $NiSe_2$ into the SnO_2 lattice, while secondary peaks indicated nanocomposite formation. HRTEM results revealed the size of the material (SnO_2: 36 nm and $NiSe_2$: 18 nm). In the DPPH scavenging studies, we optimized concentration, pH and time kinetics. The 30% $NiSe_2$-doped SnO_2 NCs showed superior activity, with an IC_{50} value of 41.2 $\mu g\ mL^{-1}$ (first-order kinetics), compared with other materials. Post-antioxidant ESR confirmed radical scavenging by NCs, and FTIR spectral results confirmed the structural rigidity of DPPH. Post-reaction XPS analysis revealed a notable change in the oxygen vacancy signal in the oxygen 1s spectrum, confirming that electron originating from an oxygen vacancy to scavenge the free radical's mechanism. Additionally, the 30% $NiSe_2$-doped SnO_2 NCs exhibited strong antibacterial activity against *K. pneumoniae*, *P. aeruginosa*, *E. coli*, and *S. aureus*, demonstrating their potential for biomedical applications.

1. Introduction

The oxidation mechanism is vital for cellular life. Aerobic cellular respiration in organisms produces energy from organic molecules like glucose while simultaneously producing free radicals that induce cellular damage during metabolism.[1] A free radical possesses an unpaired electron that is characterized by a quantum mechanical feature known as spin. This entity generally exhibits significant reactivity due to its open-shell structure.[2] The presence of free radicals is indicative of oxidative stress. Oxidative stress is relatively a new concept in medical science. It is a crucial physiological imbalance that occurs when the production of reactive oxygen species (ROS) surpasses the ability of endogenous antioxidant defences to remove them. Initially identified in the mid-20th century through the cutting-edge study of Gerschman, Harman, and others, ROS-mediated oxidative stress is now known to contribute to cellular injury, inflammation, aging, and a broad array of chronic disorders. Biological systems employ enzymatic antioxidants (SOD, CAT, and GPx) and non-enzymatic antioxidants (ascorbate, tocopherols, and glutathione)[3] to remove ROS; however, the efficacy of these small molecules is frequently ephemeral. Their swift deterioration, instability under physiological settings, and constrained diffusion-controlled radical quenching efficacy limit their prolonged therapeutic and technical applicability.[4]

These constraints prompted the investigation of solid-state antioxidants, particularly metal oxides, at the beginning of late 1990s and early 2000s, when the catalytic redox properties of CeO_2, MnO_2, and TiO_2 generated substantial interest in defect-mediated ROS regulation.[5] Metal oxides possess adjustable electronic structures, wide band gaps and enhanced surface reactivity, which contribute to their prolonged radical scavenging activitiy. Oxygen-deficient oxides have proven to be remarkably effective antioxidants. Their surface oxygen vacancies (V_O) serve as electron-rich sites that directly participate in redox reactions with ROS, simulating and even outperforming traditional antioxidant behaviour.

Department of Chemistry, College of Engineering and Technology, SRM Institute of Science and Technology, Kattankulathur–603203, Tamil Nadu, India. E-mail: devikals@srmist.edu.in

The antioxidant efficacies of metal oxides are determined by their radical scavenging processes, which generally function through electron transfer (ET), hydrogen atom transfer (HAT), or radical adduct formation (RAF).[6] In metal oxide semiconductors, electron transfer dominates due to the effects of their electronic states, redox potential, and the capacity of oxygen vacancies (V_o) to function as a readily accessible electron reservoir. The operative mechanism is not simply a descriptive element; it affects the reaction kinetics, thermodynamic viability, and selectivity for the radical species. Furthermore, this mechanistic approach directly affects essential material characteristics, including redox reversibility, defect regeneration, and long-term cycling stability, which enable solid materials to outperform conventional small molecule quenchers.

Consequently, establishing the molecular basis of ROS quenching is essential for the systematic development of next-generation antioxidant materials. A full mechanistic understanding facilitates the prediction and modification of band structures, defect chemistry, dopant distribution, and surface electronic states, consequently permitting the deliberate design of highly effective radical-capturing and -scavenging platforms. Fundamentally, mechanism-driven design converts empirical material discovery into a systematic, controllable, and performance-optimized approach for the development of improved metal oxide antioxidants.

Tin oxide (SnO_2) NPs have particularly significant chemical, electrical and optical properties. The bandgap of SnO_2 NPs ranges from 2.4 to 3.6 eV, which is characteristic to n-type semiconductors and contributes to their high optical transparency and low electrical resistivity.[7] Nano-sized SnO_2 NPs show improved photocatalytic activity due to their increased surface-to-volume ratio and enhanced surface reactivity, compared to other metal oxide semiconductors. As a result, SnO_2 NPs show extensive applicability in several technologies and research fields, such as energy storage,[8] catalysis,[9] agriculture,[10] gas sensing,[11] and solar energy conversions.[12]

Conventional procedures for synthesising SnO_2 NPs is chemically and physically intensive and may negatively impact the environment due to the high energy consumption and elevated temperatures; they also require costly processing methods and the use of hazardous solvents. To address these limitations, alternative green and environmentally friendly techniques have been developed. These techniques use biological sources such as plants, algae, and microorganisms as natural agents for reducing and capping agents, for the formation of NPs, and to reduce the use of toxic chemicals.[13] Especially, the *Justicia adhatoda* plant extract is rich in phytochemicals such as alkaloids, flavonoids, phenolics, terpenoids and secondary metabolites, which act as reducing and capping agents for NPs synthesis.[14] These systems promote the controlled nucleation and growth of the NPs, resulting in good crystallinity and enhanced surface functionality. These approaches enhance the biocompatibility and stability of NPs and provide a cost-effective and economically viable way to fabricate functional nanostructures with significant potential for use in therapeutic and catalytic applications.

In addition, nickel-based NPs have shown vital antimicrobial properties and are promising candidates for various medical, environmental, and industrial uses. Numerous studies have reported that Ni NPs can significantly inhibit the growth and reproduction of both Gram-negative and Gram-positive bacteria, demonstrating a broad range of antimicrobial activity.[15] Among nickel compounds, $NiSe_2$ in the form of NPs shines as it has attractive scientific features, such as unique magnetic, electrical and catalytic properties.[16] These properties are highly suited for different technologies and energy-based applications, such as electrochemical sensors,[17] catalysis,[18] solar cells,[19] electrolysis, optical devices and supercapacitors.[20–23] Its outstanding conductivity, strong structural integrity, and reactive surface characteristics further expand its uses.

As a vital trace element, selenium is an essential part of selenoproteins and selenium compounds in the human body.[24] Se plays a major role in metabolism, DNA synthesis, reproduction, the regulation of thyroid hormones, and the prevention of oxidative stress and infection. Due to its strong reactivity in hydration and oxidation reactions, as well as its significant photoconductivity and low melting point, Se is useful for a wide range of industrial and technological applications. The UK scientific group on vitamins and minerals advises a daily intake of selenium of around 60 μg for women and 70 μg for men.[25] However, intake surpassing 400 μg per day may lead to selenosis, a toxic condition characterized by symptoms including gastrointestinal disturbances, hair loss and nail brittleness. Thus, it is essential to sustain an optimal selenium balance to fully leverage its health advantages while preventing toxicity.[26]

In this research, we have successfully implemented an innovative strategy for the preparation of $NiSe_2$ NPs and $NiSe_2$-doped SnO_2 NCs using plant extract at various doping concentrations. Previous studies on metal oxide-based antioxidants and antibacterial materials (such as SnO_2, CeO_2, TiO_2 and ZnO)[20,27–30] primarily relied on intrinsic effects, particularly oxygen vacancies in single-component metal oxides, to explain radical scavenging and antibacterial activity. In contrast, the novelty of this work lies in the introduction of $NiSe_2$ as a dopant in the SnO_2 lattice. The NCs were employed to elucidate the most favourable mechanistic pathways governing antioxidant activity using the DPPH assay, with systematic optimization of both pH and NCs concentration, which has not been previously reported. Furthermore, the antibacterial activity of the NCs was evaluated against Gram-negative bacteria (*Klebsiella pneumoniae*, *Escherichia coli*, and *Pseudomonas aeruginosa*) and a Gram-positive bacterium (*Staphylococcus aureus*). Notably, 30% $NiSe_2$-doped SnO_2 NCs exhibited the highest performance, confirming the critical role of the optimized $NiSe_2$ incorporation.

2. Materials and experimental methods

A brief description of the materials, instrumentation, and analytical procedures is provided in the SI.

2.1. Preparation of *Justicia adhatoda* leaf extract

The leaves of *Justicia adhatoda* were collected from a local garden in Chennai, Tamil Nadu. The plant leaves were washed with tap water thrice to remove unwanted dust particles, rinsed with double-distilled water (DDW), and dried at room temperature. Subsequently, 20 g of *Justicia adhatoda* leaves were crushed and mixed with 300 mL of DDW and boiled for 25 minutes at 70 °C. After boiling, the solution was cooled to RT. The colour changed from pale green to greenish brown. The leaf extract was then filtered through Whatman No. 1 filter paper, and the resulting extract was kept at 5 °C for use in nanoparticle synthesis.

2.2. Plant-extract-mediated synthesis of SnO_2 nanoparticles

SnO_2 NPs were synthesised using the plant extract by a green method. 400 mg of tin precursor ($SnCl_4 \cdot 2H_2O$ (0.01 M)) was dissolved in 100 mL of DDW, then 50 mL of *Justicia adhatoda* leaf extract and 2 mL of ammonia solution (25%) were added to the reaction mixer to maintain pH 8, and the mixture was stirred at RT. The solution was centrifuged at 4000 rpm for 15 min, and the resulting precipitate was washed three times with DDW and ethanol and dried at 110 °C overnight to obtain the plant-extract-based SnO_2 NPs, with a reaction conversion of ~88%.

2.3. Biosynthesis of $NiSe_2$ nanoparticles

The $NiSe_2$ NPs were synthesised by a wet chemical method. First, 581 mg of nickel precursor (Ni $(NO_3)_2 \cdot 6H_2O$ (0.01 M)) was dissolved in 200 mL of DDW, followed by the addition of 50 mL of *Justicia adhatoda* leaf extract, and the mixture was stirred at RT for 30 min to obtain a solution (solution-A). Then, 395 mg of selenium ultra-pure powder (0.1 M) was dissolved in 50 mL of leaf extract along with ammonia solution (solution-B), stirred at RT for 30 min. Solutions A and B were then blended together to form a homogenous mixture. Subsequently, 50 mL of *Justicia adhatoda* leaf extract was added as a stabilizing agent. Followed by heating at RT and stirred for 2 hours, later it was centrifuged at 4000 rpm for 10 min and the precipitate was rinsed three times with DDW and ethanol. Finally, the product was dried overnight at 110 °C to obtain ultra-pure $NiSe_2$ NPs *via* a bio-synthesis method, achieving a reaction conversion of approximately 75%.

2.4. Ultrasonic-assisted synthesis of the $NiSe_2$-doped SnO_2 nanocomposite

In this process, 10 mg of nickel selenide ($NiSe_2$) NPs were first dispersed in 50 mL of ethanol, after which 90 mg of plant-

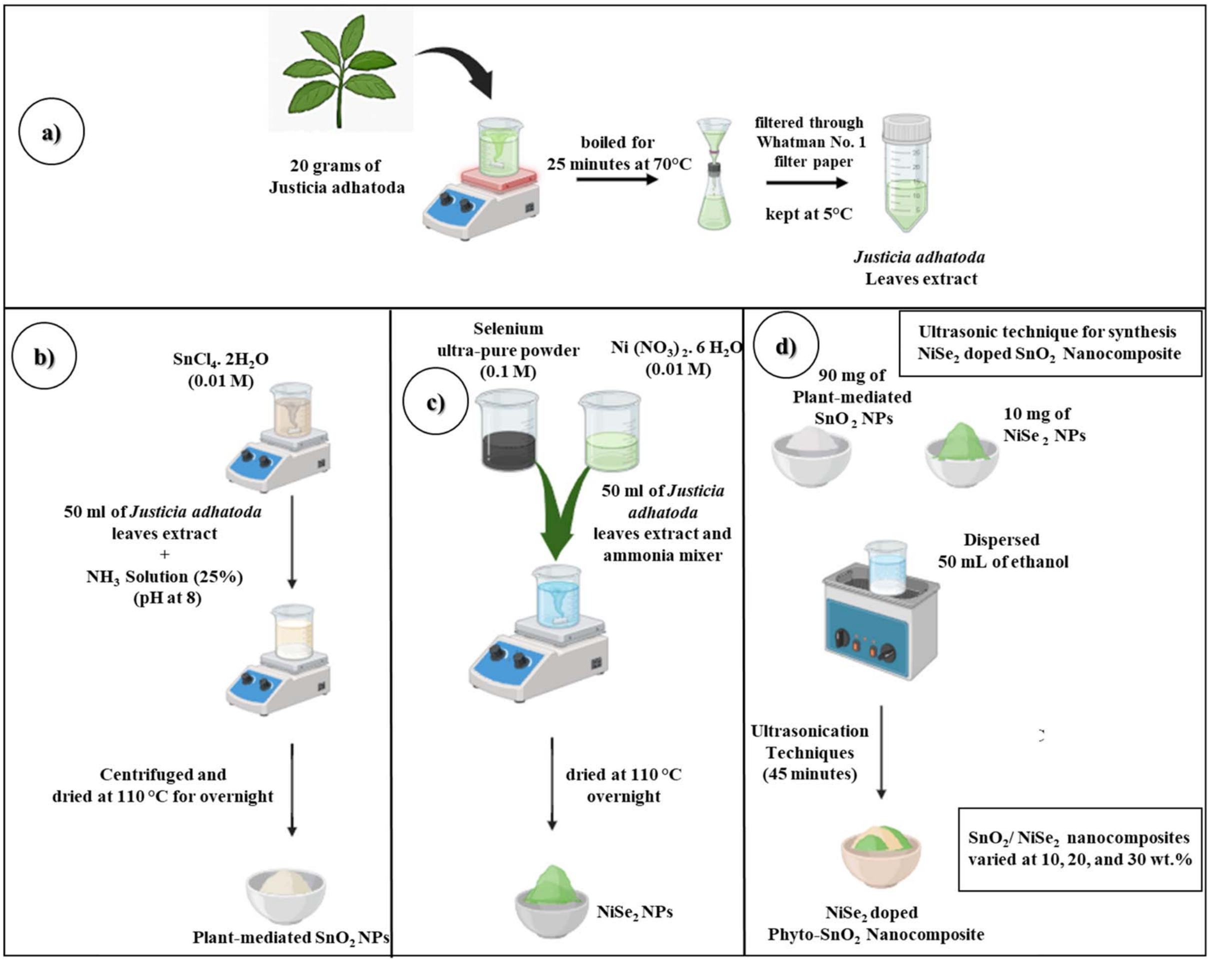

Scheme 1 Schematic illustration of the synthesis of SnO_2 and $NiSe_2$-doped SnO_2 nanocomposites: (a) preparation of *Justicia adhatoda* leaf extract, (b) green synthesis of plant-mediated SnO_2 nanoparticles, (c) synthesis of $NiSe_2$ nanoparticles using the leaf extract, and (d) ultrasonic fabrication of $NiSe_2$-doped SnO_2 nanocomposites with varying $NiSe_2$ concentrations (10, 20, and 30 wt%).

mediated stannous oxide (SnO_2) NPs was added, and ultrasonication was applied to the slurry for 45 minutes to ensure thorough mixing. The mixture was then dried overnight at 110 °C to obtain $NiSe_2$-doped SnO_2 NCs. The nickel selenide ($NiSe_2$) NPs had varied concentrations (10, 20, and 30 wt%) relative to SnO_2 to synthesise $NiSe_2$-doped SnO_2 NCs (Scheme 1).

3. Results and discussions

3.1. Structural and morphological characterizations

XRD analysis was performed to determine the crystallinity of SnO_2, $NiSe_2$ and the $NiSe_2$-doped SnO_2 NCs. The XRD pattern of SnO_2 NPs showed distinct peaks at $2\theta = 26.67°$, 34.50°, 38.07°, 43.51°, 51.85°, 54.74°, 58.65°, 62.06°, 65.62°, and 78.38° corresponding to the (110), (101), (200), (210), (211), (220), (002), (310), (112), and (321) Bragg reflections, respectively, which is in perfect agreement with the dominant phase corresponding to the SnO_2 NPs (JCPDS card no. 41-1445, tetragonal structure).[31] The green-synthesised $NiSe_2$ NPs exhibited strong intensity peaks at 30.57°, 34.16°, 37.04°, 43.35°, 51.85°, 56.28°, 60.18°, and 74.14° corresponds to (111), (220), (210), (211), (220), (311), (400), and (421) planes, respectively, which correspond to the cubic phase of penroseite, which is similar to the pyrite structure (JCPDS card no. 00-011-0552).[32] The peak at 26.34° occurs due to selenium. After doping $NiSe_2$ onto SnO_2 NPs, the XRD peak of SnO_2 at 26.67° shifts towards lower values and higher values, as shown in Fig. 1a and b. This was the strongest evidence that $NiSe_2$ was effectively doped into SnO_2 NPs. Rietveld refinement was carried out for the pristine SnO_2 and $NiSe_2$ samples to confirm the phase purity. The refinement was performed using the rutile SnO_2 structure ($P4_2/mm$) and the cubic $NiSe_2$ structure ($Pa\bar{3}$), resulting in an excellent agreement between the experimental and calculated profiles (Fig. S3.1); the results demonstrate the purity of the material.

After effective doping, the dopant material can alter the crystal parameters, including lattice parameters, average crystallite size, cell volume, X-ray density, average crystalline size, atomic packing fraction, and surface-to-volume ratio, as detailed in Table 1.

The average crystallite size of the synthesised materials was calculated using Scherrer's eqn (1).

$$D = \frac{k\lambda}{\beta}\cos\theta \tag{1}$$

where, D is the average crystallite size of the crystal in nm, λ is the X-ray wavelength (1.5405 Å with Cu Kα), θ is the Bragg angle, β is the full width at half-maximum in radians, and k is a shape factor (0.9).

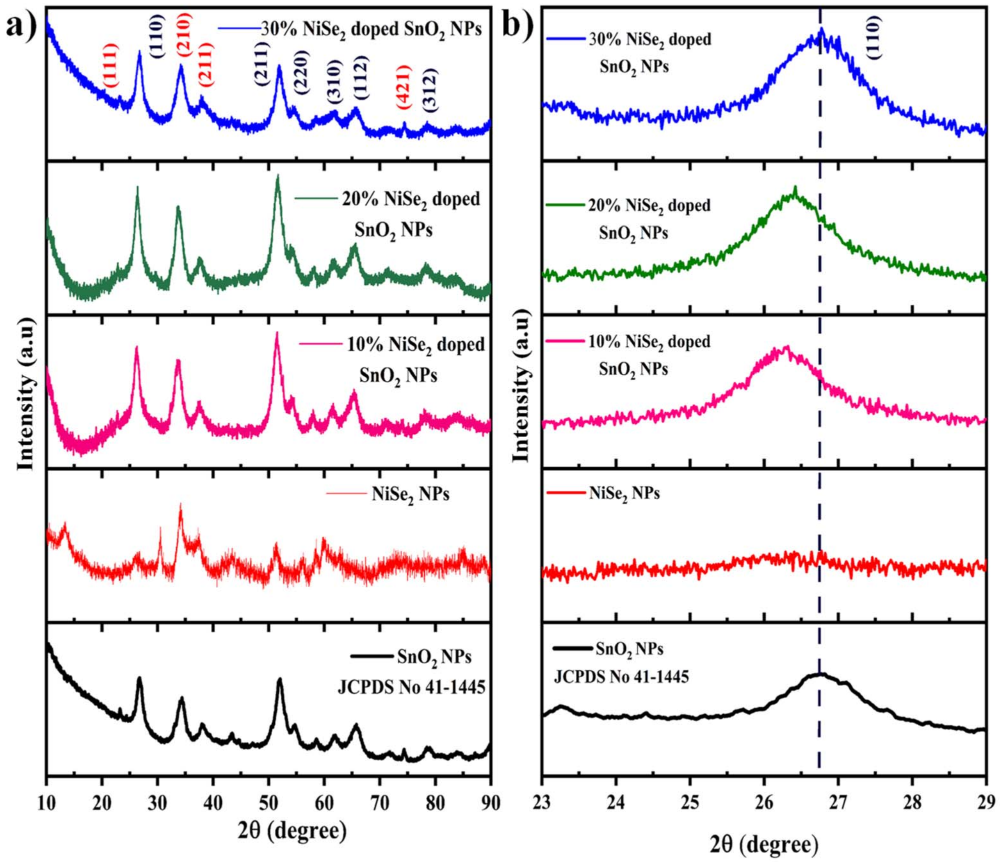

Fig. 1 (a) XRD patterns of the synthesised SnO_2 NPs and $NiSe_2$-doped SnO_2 NCs at different concentrations (10%, 20%, and 30%). (b) Peak shift of the dominant (110) plane with increasing $NiSe_2$ concentration.

Table 1 Comparison of XRD parameters (lattice parameters, cell volume, X-ray density, atomic packing fraction and crystalline size) pre- and post-reaction of $NiSe_2$-doped SnO_2 NCs at different concentrations (10%, 20%, and 30%)

		Lattice parameters (Å)				Cell volume (Å^3)		X-ray density (g cm^{-3})		Atomic packing fraction (APF)		Crystalline size (nm)	
		Pre		Post									
Sl. no.	Materials	*a*	*c*	*a*	*c*	Pre	Post	Pre	Post	Pre	Post	Pre	Post
1	SnO_2 NPs	4.738	3.187	4.750	2.653	69.190	59.87	7.23	8.37	0.524	0.813	8.17	17.56
2	10% $NiSe_2$-doped SnO_2 NCs	4.787	3.196	4.477	2.668	73.225	60.71	7.13	8.60	0.627	0.938	14.66	17.22
3	20% $NiSe_2$-doped SnO_2 NCs	4.767	3.192	4.782	2.665	72.548	60.95	7.50	8.93	0.766	1.069	13.63	6.97
4	30% $NiSe_2$-doped SnO_2 NCs	4.704	3.157	4.038	1.579	69.847	25.75	8.11	21.98	0.706	2.85	16.98	22.57

The average crystallite size of SnO_2 is 8 nm. After $NiSe_2$ was doped into SnO_2 NPs, the average crystallite size increased when compared to SnO_2 NPs. The NCs range in size from 8 to 17 nm, which may be due to $NiSe_2$ expanding the crystal lattice of SnO_2 NPs.

The lattice parameters of the material *a* and *c* were calculated from eqn (2).

$$\frac{1}{d^2} = \frac{h^2 + k^2}{a^2} + \frac{l^2}{c^2} \tag{2}$$

where, *a* and *c* are the lattice parameters, *d* is an interplanar distance, and (*hkl*) are the Miller indices. The lattice parameters gradually increase with increasing $NiSe_2$ content into the SnO_2 NPs due to ionic size differences. While Sn^{+IV} and Ni^{+II} possess comparable ionic radii, (∼69 pm), the anions different significantly, the Se^{-II} ions (∼198 pm) is much larger than O^{-II} ions (∼140 pm). This size mismatch induces lattice distortion in the crystal structure. However, the lattice parameters increase as the concentration of $NiSe_2$ increases. This behaviour is not observed for 20% and 30% $NiSe_2$-doped SnO_2 NCs. At lower concentrations, the dopant ions is readily substituted into the lattice sites, resulting in minimal lattice expansion. However, at higher concentrations, interstitial incorporation or secondary phase formation may occur, leading to structural distortion. The crystal becomes distorted or strained in the lattice, and the parameters decrease, as shown in Fig. 2a.

The volume of the unit cell and X-ray density were calculated using eqn (3).

$$V = a^2 \times c \tag{3}$$

where *a* and *c* are lattice parameters. The volume of the unit cell increases at lower concentrations, while the cell volume decreases as the concentration increases due to different lattice parameters. These values are listed in Table 1. The X-ray density was determined by eqn (4).

$$P_x = \frac{nM}{N_A V} \tag{4}$$

where *n* is the number of atoms per unit cell, *M* is the molecular weight of the material, N_A is the Avogadro number, and *V* is the volume of the unit cell. The X-ray density decreases at lower concentrations of $NiSe_2$-doped SnO_2 NCs. When the $NiSe_2$ concentration increases, the X-ray density increases. This may be due to the decrease in the volume of the cell unit as the molecular weight of the nanocomposite increases. The molecular weight of SnO_2 is 150.71 g mol^{-1} and that of $NiSe_2$ is 216.61 g mol^{-1}. The volume unit cell decreases, and X-ray density increases, with increasing $NiSe_2$ concentration, as shown in Fig. 2b. This means that the Ni and Se ions are effectively doped into the Sn and O sites of the SnO_2 structure.

The atomic packing fraction (APF) was calculated using eqn (5).

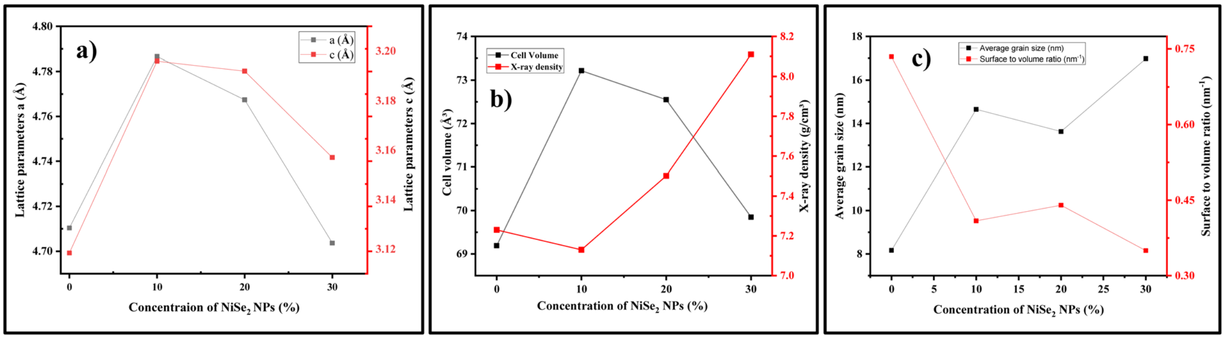

Fig. 2 (a) Lattice parameters [a and c], (b) unit cell volume and X-ray density, and (c) average grain size and surface to volume ratio of the undoped SnO_2 NPs and $NiSe_2$-doped SnO_2 NCs at different concentrations (10%, 20% and 30%).

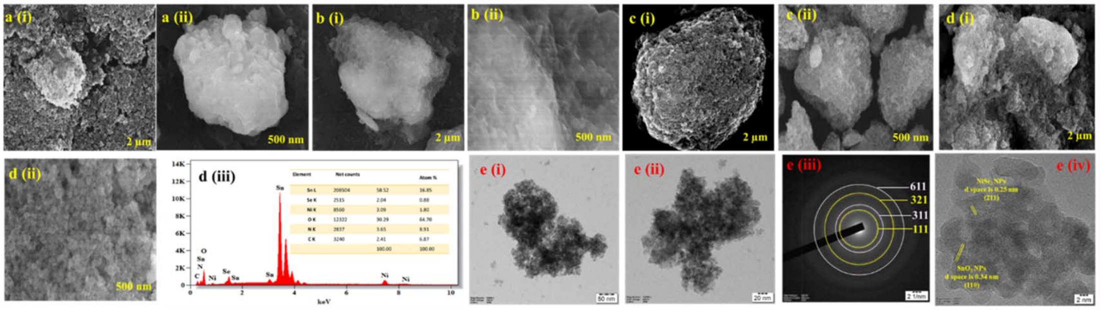

Fig. 3 (a(i and ii)) SEM image of SnO_2 NPs; (b–d(i and ii)) SEM image 10%, 20% and 30% $NiSe_2$-doped SnO_2 NCs at magnification of 2 μm and 500 nm; (d(iii)) EDS spectrum of 30% $NiSe_2$-doped SnO_2 NCs; (e(i and ii)) TEM images at different magnifications (50 and 20 nm), (e(iii)) SAED pattern, and (e(iv)) HRTEM image showing lattice fringes and *d* space values of of 30% $NiSe_2$-doepd SnO_2 NCs.

$$\mathrm{APF} = \frac{\frac{4}{3}\pi r^3 n}{V} \tag{5}$$

The atomic packing factor (APF) of the $NiSe_2$-doped SnO_2 NCs exhibited a clear dependence on dopant concentration. At lower $NiSe_2$ concentrations, the APF values increased, which may be attributed to the reduction of interstitial voids and homogeneous substitution of Ni and Se ions within the SnO_2 lattice. Such uniform incorporation improves the local atomic packing efficiency without significant structural distortion. However, at higher doping levels (≥30%), the APF values decreased markedly (Fig. 2c), indicating severe lattice distortion, crystal strain, and the generation of oxygen vacancies caused by excessive dopant incorporation.

The morphological (shape) and elemental composition of green-synthesised SnO_2, $NiSe_2$ NPs and $NiSe_2$-doped SnO_2 NCs were investigated by HRTEM and FESEM-EDAX analysis. The

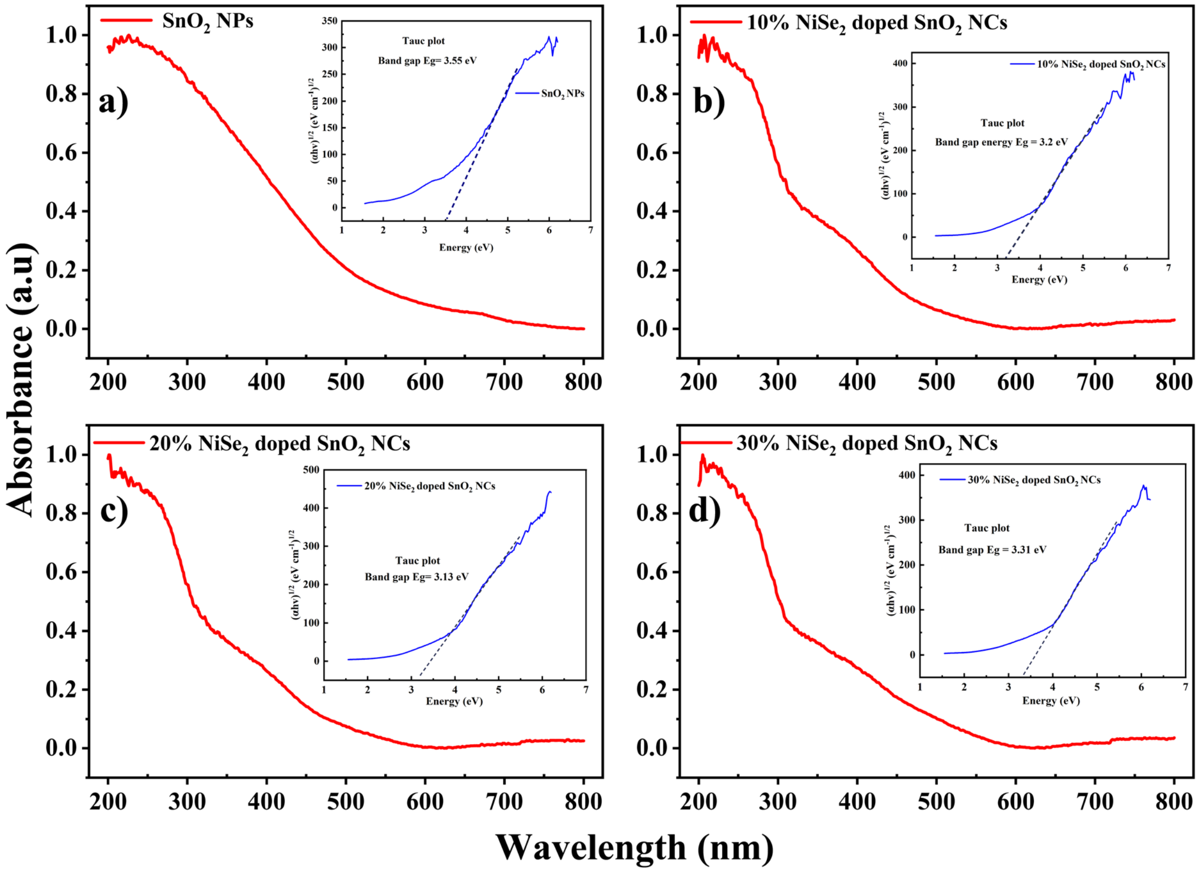

Fig. 4 UV-visible spectra and Tauc plots (insets) for (a) undoped SnO_2 and (b–d) $NiSe_2$-doped SnO_2 NCs at different concentrations (10%, 20%, and 30%).

images were recorded at magnifications of 2 μm and 500 nm. The green synthesised undoped SnO_2 NPs were not uniformly distributed and exhibited significant aggregation, forming irregular and clustered spherical particles, as shown in Fig. 3a(i and ii). The $NiSe_2$ particles exhibited an irregular spherical cluster-like morphology. After doping $NiSe_2$ NPs into SnO_2 NPs, the $NiSe_2$ surrounded and embedded the surface of SnO_2 NPs, as shown in Fig. 3b and c(i and ii); this was confirmed by FESEM analysis. The shape of the NPs plays a crucial role in determining their efficacy against pathogens; spherical NPs tend to be very potent during antibacterial activity owing to their ability to easily penetrate into the cell wall of pathogens. After doping, the dopant materials are embedded on the surface of the irregular spherical shape. It effectively interacts with bacterial cells, thereby enhancing its antibacterial efficiency. EDS analysis of 30% $NiSe_2$-doped SnO_2 NCs confirmed that $NiSe_2$ was evenly distributed on the surface of SnO_2 NPs, as shown in Fig. 5b(i–viii).

HRTEM analysis of the 30% $NiSe_2$-doped SnO_2 NCs shows that spherical SnO_2 NPs were surrounded by small spherical $NiSe_2$ NPs, with a cluster-like morphology. SAED pattern analysis demonstrated excellent agreement with the XRD data, and the *d*-space values were perfectly matched with those of SnO_2 and $NiSe_2$ NPs with corresponding planes, as shown in Fig. 3e(iii–iv). The average particle size was determined to be 36 nm (SnO_2) and 18 nm ($NiSe_2$) by particle size distribution spectra, as shown in Fig. S3.2. It was evident from the results that the size of the $NiSe_2$ NPs was much smaller than that of the SnO_2 NPs.

UV-visible spectroscopy was used to determine the optical properties of the synthesised materials. Fig. 4 shows the UV-vis spectra of SnO_2 and $NiSe_2$-doped SnO_2 NCs. The optical bandgap values were calculated using Tauc–Lorentz eqn (6),[33] which correlates the incident photon energy with the absorption coefficient:

$$\alpha h\nu = A(h\nu - E_g)n \tag{6}$$

where *n* is the optical bandgap, in direct bandgap semiconductors, *n* is the power of $(h\nu - E_g)$, where *h* is the frequency and E_g is the bandgap ($n = 1/2$). These predicted band gaps of SnO_2 NPs were found to be approximately 3.5 eV. With the incorporation of lower concentrations of $NiSe_2$ into the SnO_2 crystal, the absorption edge is expanded within the visible spectrum, and a significant redshift is observed. The redshift could result from defect states introduced by Ni/Se doping and oxygen vacancies within the band gap of the host material, reducing its effective band gap energy. Because $NiSe_2$ is incorporated into SnO_2, the Ni 3d and Se 4p orbitals interact with Sn 5s/5p and O 2p orbitals, causing sp–d and p–p hybridization.[34] This interaction, along with crystal imperfections, such as oxygen vacancies or Sn interstitials, can introduce defect states within the band gap. These defect states shift the Fermi level and effectively narrow the band gap. Accordingly, the bandgap values for 10% and 20% $NiSe_2$-doped SnO_2 NCs are 3.13 and 3.2 eV, respectively.

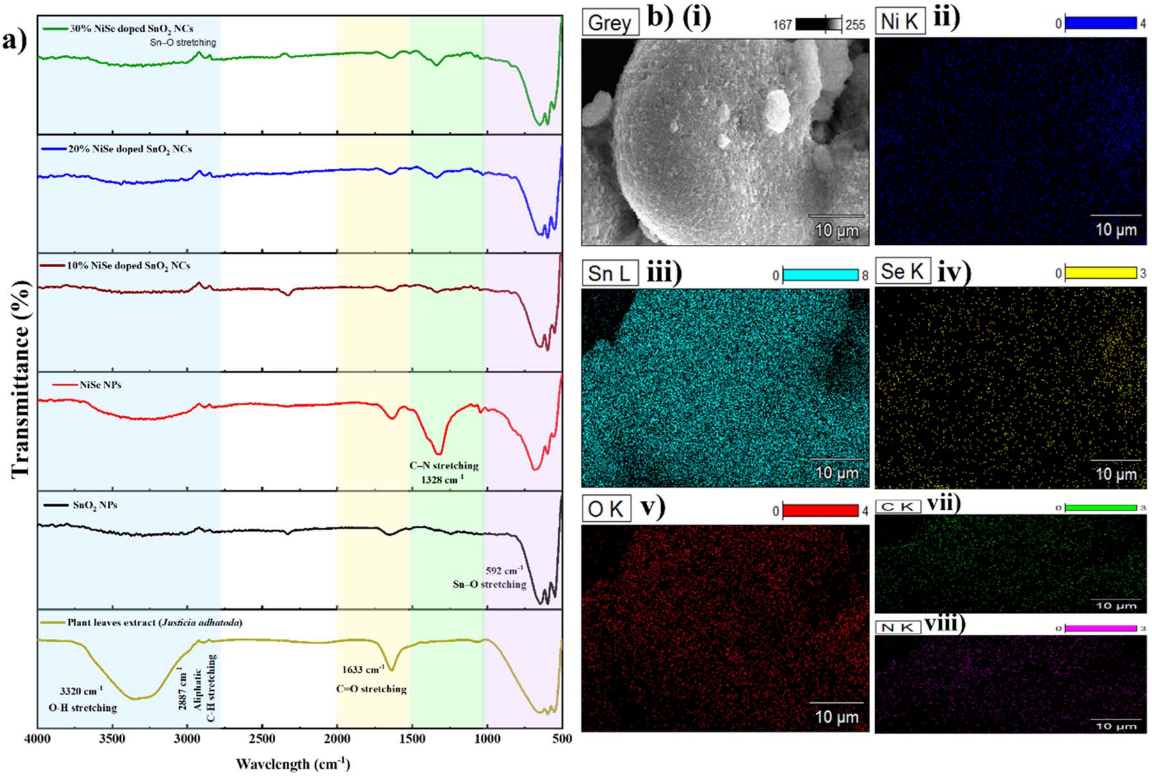

Fig. 5 (a) FTIR spectra of the synthesised undoped SnO_2 NPs and $NiSe_2$-doped SnO_2 NCs at various concentrations (10%, 20% and 30%) and (b) (i–viii) EDS elemental mapping images of 30% $NiSe_2$-doped SnO_2 NCs.

At higher concentrations of $NiSe_2$ in SnO_2, the parent material becomes overloaded, and strain and distortion are introduced due to ionic radius mismatch ($Ni^{+II} < Sn^{+IV}$, $Se^{-II} > O^{-II}$). This lattice mismatch disturbs the orbital alignment and reduces structural symmetry, leading to phase segregation. The weakened orbital overlap suppresses effective s–p and p–p hybridization,[35] resulting in band gap widening to approximately 3.31 eV.

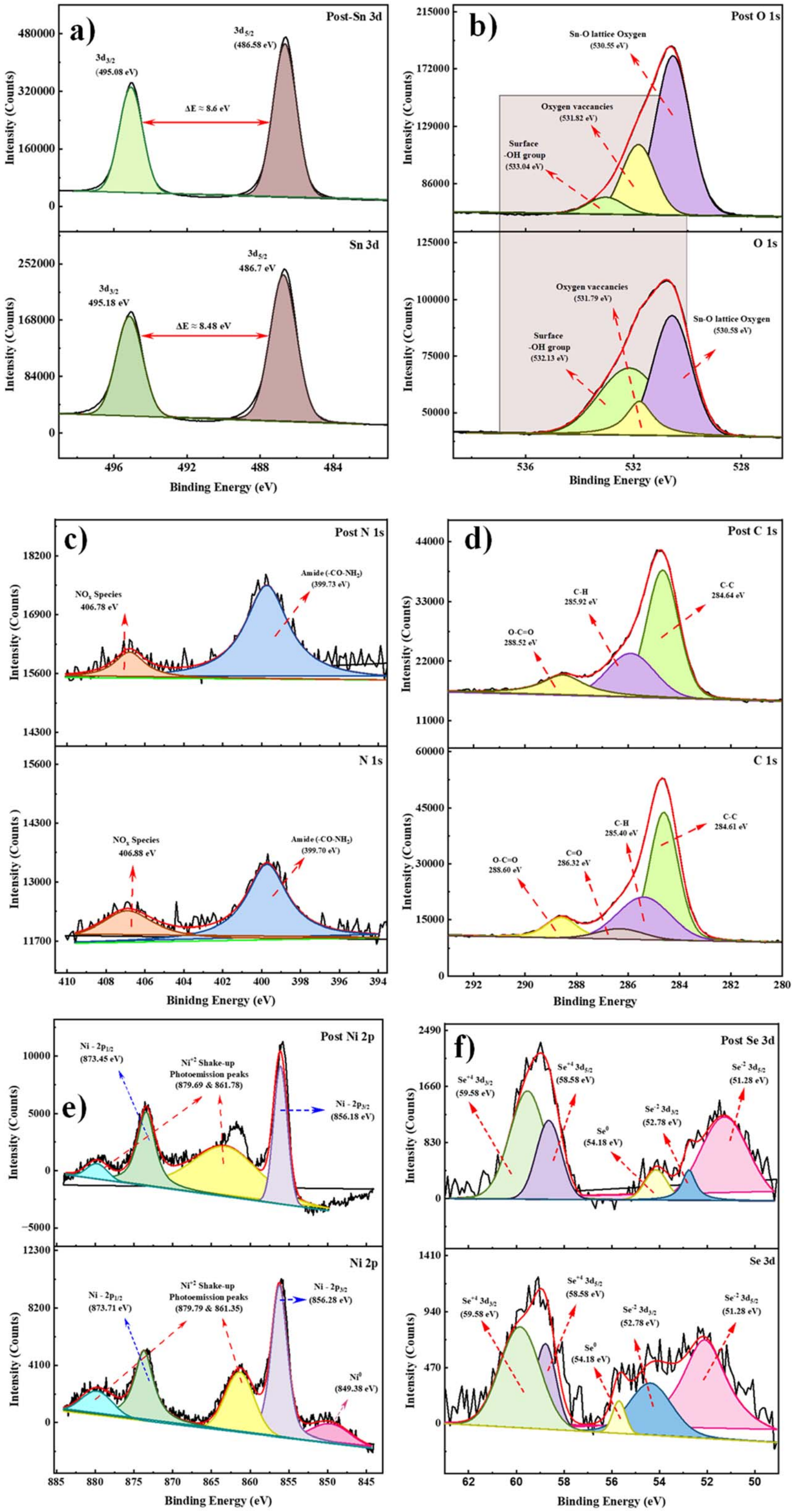

Fig. 6 (a–f) Pre- and post-reaction XPS spectra of 30% $NiSe_2$-doped SnO_2 NCs showing the core levels of Sn, O, Ni, and Se.

The FTIR spectra of undoped SnO_2 and $NiSe_2$-doped SnO_2 NCs are shown in Fig. 5. The plant extract (*J. adhatoda*) showed peaks at 3320, 2887, and 1633 cm^{-1}. The peaks correspond to O–H bond, aromatic C–H stretching, and carbonyl groups, respectively. The undoped SnO_2 NPs exhibit peaks at 3320, 2887, 1633 and 592 cm^{-1} corresponding to OH, CH, CO, and SnO_2 groups, respectively. These peaks were used to confirm the presence of *J. adhatoda*-mediated undoped SnO_2 NPs. The FTIR peaks of $NiSe_2$ were largely similar to those of the plant extract, with an additional peak at 1328 cm^{-1}, attributed to C–N stretching vibration of phytochemical residue. Most of the peaks in the FTIR spectrum of $NiSe_2$-doped SnO_2 NCs at different concentrations (10, 20 and 30%) were similar to those of the plant extract, with an additional peak at 1328 cm^{-1}, attributed to C–N stretching, as shown in Fig. 5a. Increasing the $NiSe_2$ concentration (10–30%) enhances the C–N peak intensity, indicating stronger interaction between dopant species and surface nitrogen functionalities. Higher $NiSe_2$ content likely induces lattice distortion and increases polarizability, promoting more effective adsorption or coordination of phytochemicals, thereby reinforcing surface biofunctionalization and potentially improving nanocomposite reactivity.

The zeta potential of SnO_2 NPs is approximately 25 mV, and it is positively charged. This positive charge is the result of two primary contributions: (1) the hydrolysis of the precursor results in the formation of protonated hydroxyl groups ($-OH_2^+$) and the presence of Sn^{+IV} cations on the material surface. (2) Functional groups can undergo protonation in aqueous environments where the phytochemicals are present on the material's surface. The agglomeration of the NPs was effectively inhibited by the electrostatic repulsion generated by the presence of positively charged groups. After adding $NiSe_2$ (lower concentration), the ZP value decreased slightly compared to that of SnO_2, to a potential value of around 18.5 mV. This reduction indicates partial neutralization of surface positive charge; this effect arises from substitutions of Sn^{+IV} with Ni^{+II} ions and Se^{-II} introduced in the undoped SnO_2 NPs, both of which lower the net positive charge density on the nanoparticle surface. In addition, the phytochemical capping agents from the *Justicia adhatoda* extract may interact differently with the doped surface, further reducing surface protonation. Although the potential decreases, the value (+18.5 mV) remains sufficiently positive to impart moderate colloidal stability through electrostatic repulsion. When higher concentrations of $NiSe_2$ were doped into SnO_2 NPs, the zeta potential value slightly increased compared to undoped and less $NiSe_2$-doped NCs (10% $NiSe_2$-doped SnO_2 NCs ZP value around 29.8 mV, and 30% $NiSe_2$-doped SnO_2 NCs ZP value around +37.7 mV). This is slightly different from previous trends due to changes in surface chemistry rather than bulk stoichiometry alone. At high dopant concentrations, Ni species are more likely to segregate toward the nanoparticle surface or form Ni-rich surface phases. These sites present labile hydroxyl groups that are easily protonated under the experimental conditions, thereby increasing the net positive charge, as shown in Fig. 7a. In addition, excess $NiSe_2$ may disrupt or displace certain phytochemical capping agents derived from *Justicia adhatoda*. Since some of these biomolecules carry negatively charged or deprotonated functional groups that mask surface cations at low doping, their partial removal would expose more positively charged Sn^{+IV} and Ni^{+II} sites, further enhancing the surface potential. Phase segregation occurs as the Se^{-II} anions migrate to the particle lattice, leaving the outer surface filled with cationic species. These factors explain the reason for the increase in the surface charge at higher concentrations of $NiSe_2$ doping.

The survey spectrum of the synthesised NCs is shown in Fig. S3.3. Elements such as Ni, Se, Sn, O, N and C are present in the NCs. The signals of carbon and nitrogen are obtained from the leaf extract of *Justicia adhatoda*, which is employed in the synthesis process. The core material in our NCs is Sn, and its 3d spectrum contains two distinct peaks at 495.15 eV and 486.7 eV, which correspond to Sn $3d_{3/2}$ and Sn $3d_{5/2}$, respectively, with a spin–orbit splitting (ΔE) of around 8.48 eV (Fig. 6a). The observed peak separation corresponds to tin existing in a +IV

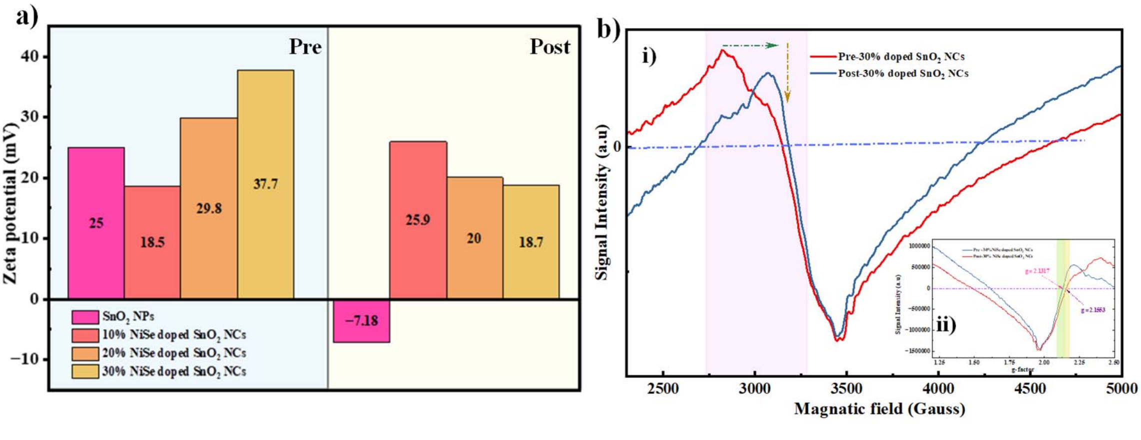

Fig. 7 (a) Zeta potential characterization of the undoped SnO_2 NPs and $NiSe_2$-doped SnO_2 NCs at different concentrations (10%, 20, 30%) pre- and post-reaction. (b) (i and ii) ESR spectra and corresponding *g*-factor values of 30% $NiSe_2$-doped SnO_2 NCs pre- and post-reaction.

oxidation state in SnO_2.[36] A significant peak at 530.58 eV in the oxygen spectrum corresponds to lattice oxygen (M–O) with Sn–O bonding. The 531.79 eV components represent oxygen vacancies, while the 532.13 eV component represents surface hydroxyl (–OH) groups.[37–39] The C 1s spectrum, shown in Fig. 6d, reveals peaks at 284.59, 285.39, 286.35, and 288.63 eV corresponding to C–C, C–H, C═O, and O–C═O (ester-type) species, respectively. The N 1s spectrum shows an amide-like characteristic at 400 eV, as well as an additional peak at 406 eV that corresponds to surface NOx species, as shown in Fig. 6c. The presence of nitrogen and carbon species in the *Justicia adhatoda* extract is confirmed by the FTIR results shown in Fig. 5a. The high-resolution Ni 2p spectrum was deconvoluted into five distinct peaks. The lower binding energy peak at 849 eV indicates metallic Ni^0, whereas the peaks at 856.24 eV (Ni $2p_{3/2}$) and 873 eV (Ni $2p_{1/2}$) indicate the presence of Ni^{+II} oxidation states. The two additional photoemission peaks observed at 861.40 eV and 879.9 eV correspond to Ni^{+II} satellite peaks (Fig. 6e). The Se 3d spectrum shows five unique peaks (Fig. 6f). The peaks at 51.98 and 54.38 eV correspond to Se $3d_{5/2}$ and Se $3d_{1/2}$ Se^{-II} species, respectively, showing the presence of a metal–selenide bond. The signal around 55.68 eV corresponds to elemental selenium (Se^0), indicating the presence of Se–Se bonds in the metal–selenide framework. The higher binding energy maxima at 58.78 eV and 59.88 eV correspond to oxidized selenium species ($Se–O_x$) arising from surface oxygen processes.

The combined spectroscopic characterizations provide a comprehensive understanding of the synthesised NCs. The XRD patterns confirm the crystal nature and phase purity of the synthesised SnO_2 and $NiSe_2$ NPs. The characteristic peak shifts indicate that the $NiSe_2$ was effectively doped on the SnO_2 lattice; in our case, shifts to both lower and higher angles are observed due to crystal expansion and compression. The band gap alterations were confirmed by UV-visible spectroscopy. At lower concentrations, the band gap decreases, and at higher concentrations, the band gap increases due to the mismatch of ionic radius ($Ni^{+II} < Sn^{+IV}$, $Se^{-II} > O^{-II}$). The SEM and TEM analyses reveal morphological changes upon doping, consistent with the elemental composition and distribution confirmed by EDS analysis. According to the XPS results, the oxidation states of the elements Sn (Sn^{+IV}), Ni (Ni^{+II}), and Se (Se_2^{-II}) confirm the successful doping and the chemical environment of the elements. The FTIR spectra confirm the presence of functional groups in the plant extract on the surface of the NPs, indicating their role in surface capping and stabilization. The zeta potential analysis reveals that the surface charge is positive for SnO_2 NPs and that, after doping, the surface charge decreases. This likely contributes to the biological and catalytic activity. Collectively, the results of these multiple techniques corroborated the structural and compositional modifications that were responsible for the observed enhancement in the antibacterial and antioxidant activities.

The ESR spectra of pure SnO_2 reported in the literature generally exhibit a center around $g \approx 2.00$, which is frequently linked to centers related to oxygen vacancies.[40] The 30% $NiSe_2$-doped SnO_2 NCs analysed in this study showed a pre-characterization *g*-value of 2.1317, which is slightly higher than that of undoped SnO_2. The observed increase can be linked to the substitution of Ni^{+II}/Se^{-II}, lattice distortion, and the effects of enhanced spin–orbit coupling within the host matrix. Following characterization, specifically after the interaction with DPPH radicals, the *g*-value exhibited a further shift to 2.1553. The local electrical environment of the paramagnetic centers changed significantly, as evidenced by the observed upward shift in the spectral features. This shift indicates the formation of additional oxygen vacancies and surface defects states. These defects enhance the radical scavenging activity of the NPs in the DPPH assay by donating electrons and promoting surface redox reactions. The new paramagnetic centers alter the resonance state and cause increases in the g-values by changing the orbital overlap and spin distribution. This fact increases the *g*-value from 2.1317 (pre) to 2.1553 (post characterization), as shown in Fig. 7b(i and ii). It suggests electronic rearrangements and defect generation caused by interactions with the DPPH radical. The actions of these particles further support their potential for antioxidant and related functional applications.

Mechanistic insights from Post-Characterization Studies, XRD shows that DPPH incorporation and increasing $NiSe_2$ loading perturb the SnO_2 lattice in a concentration dependent manner. At low dopant concentrations (10–20%), the diffraction peaks shift slightly toward lower 2θ (lattice expansion), while peak intensities decrease, consistent with homogeneous substitution of Ni/Se into the SnO_2 lattice, moderate lattice strain, and partial loss of long-range order due to surface adsorption of organic radicals. These substitutions increase the local atomic density and reduce open interstitial voids, producing a modest increase in the apparent packing efficiency. At the highest loading (30% $NiSe_2$), the diffraction pattern changes dramatically: major peaks (*e.g.*, near $2\theta \approx 26.7°$ and $34.5°$) shift to higher angles in Fig. 8a, intensities and extracted unit cell volume collapse, and derived parameters (X-ray density, APF, crystallite size) change nonlinearly. This behaviour is indicative of severe lattice distortion, phase segregation or the formation of Ni/Se-rich secondary phases, accompanied by crystal strain and oxygen-vacancy formation. Note that geometric APF values of >1 are artefacts of the hard-sphere approximation combined with large volume changes and should be interpreted qualitatively as markers of extreme local densification or structural reorganisation rather than literal physically possible packing efficiencies; the values are denoted in Table 1. Upon interaction with the DPPH radical solution, the post-reaction zeta potential values (Fig. 7a) exhibited a significant negative shift, reaching −7.18 mV for SnO_2, and −25.9, −20, and −18.7 mV for 10%, 20%, and 30% $NiSe_2$-doped SnO_2 NCs, respectively. The reduction in surface charge magnitude after DPPH incorporation suggests surface neutralization due to adsorption of DPPH or its reduced form (DPPH–H) onto the nanoparticle surface. This modification supports the electron transport from the NPs to the DPPH radicals and demonstrates that surface oxygen vacancies and active sites are involved in the free-radical scavenging mechanism. SEM images in Fig. 8c–f show that the $NiSe_2$-doped SnO_2 NCs agglomeration after DPPH treatment compared to the pre SEM images. This aggregation is attributed to enhanced van der Waals attractions and increased

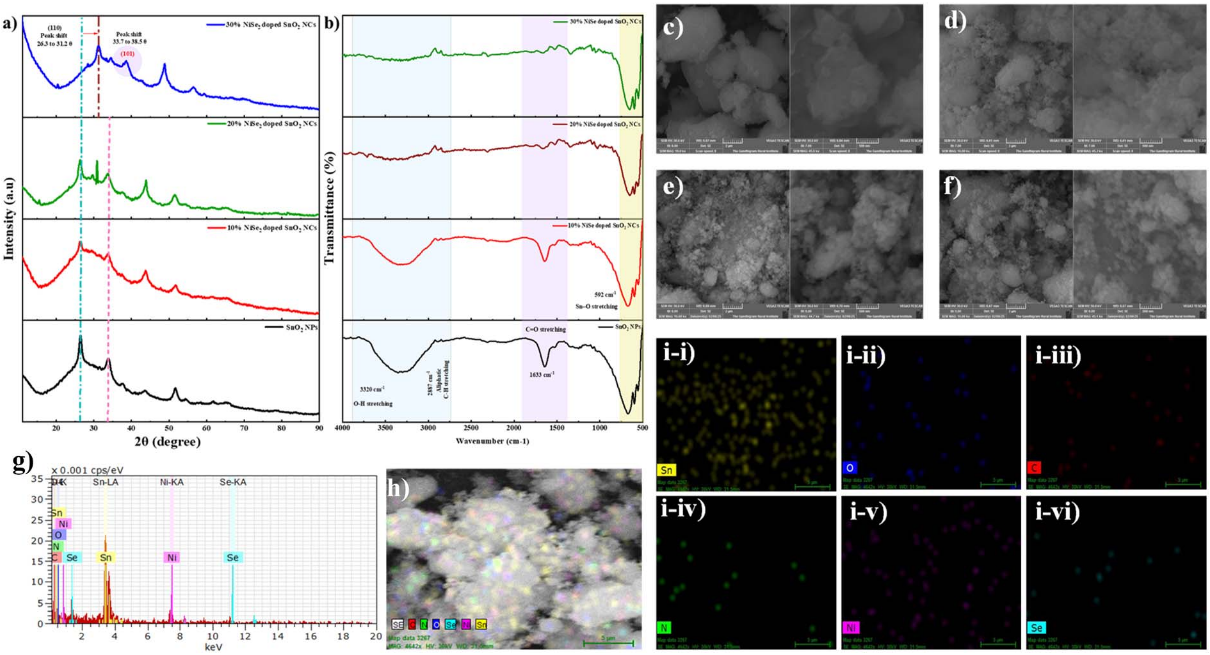

Fig. 8 (a and b) XRD and FTIR analyses performed after activity. (c–f) SEM images of SnO_2 NPs and $NiSe_2$-doped SnO_2 NCs (10%, 20% and 30%) at different magnifications (2 μm and 500 nm). (g and h [i–vi]) EDS mapping analysis of 30% $NiSe_2$-doped SnO_2 NCs.

interactions among them, it is responsible for agglomeration behaviour. Moreover, the high surface energy and presence of oxygen vacancies (V_O) on the SnO_2 surface promote interparticle adhesion through electrostatic and hydrogen-bond interactions. This aggregation, which reduces the visible surface area, might increase interfacial charge transfer in redox processes by forming conductive networks between neighbouring particles. This interfacial heterojunction architecture may thus lead to effective electron transport across the $NiSe_2$-doped SnO_2 NCs, thereby supporting increasing antioxidant and antibacterial performance. The FTIR spectra of the NCs (Fig. 8b) exhibit no notable changes before and after the DPPH interaction. This indicates that the chemical state of the NCs remains unchanged and no new bonds are formed during the radical scavenging processes. Similarly, the XPS survey and high-resolution spectra of Sn, Ni, and Se show nearly identical peak positions before and after DPPH treatment, as shown in Fig. 6a–f. This shows that the chemical states of the NCs are chemically stable. However, a noticeable variation was observed in the O 1s spectrum post reaction, as shown in Fig. 6b, where the intensity and deconvolution profile of the oxygen components decreased after DPPH incorporation. This reduction in the relative area of lattice oxygen and defect-related oxygen peaks suggests partial consumption or passivation of surface oxygen vacancies during the free-radical scavenging process. These vacancies likely participate as active sites, donating electrons to neutralize DPPH radicals, leading to a decrease in their concentration after the reaction. The XPS peak area ratio, calculated according to eqn (6), was used to estimate the relative oxygen vacancy:[41]

$$\text{Relative oxygen vaccancy ratio} = \frac{O_v}{O_L + O_v} \tag{7}$$

where O_V and O_L correspond to oxygen vacancy related and lattice oxygen species, respectively. Although this ratio does not represent the absolute oxygen vacancy density, it serves as a semiquantitative indicator of surface-defect concentration. For the 30% $NiSe_2$-doped SnO_2 NCs, the relative oxygen vacancy (ROV) increased from 0.612 before the DPPH assay to 0.626 after the assay, indicating dynamic redistribution and active involvement of surface oxygen vacancies during the radical scavenging reaction. This increase in relative oxygen vacancies corresponds to decrease in IC_{50}, suggesting that oxygen vacancies act as electron donating sites that facilitate defect assistant electron transfer to DPPH radicals. Therefore, the enhanced antioxidant performance is attributed to surface defect participation rather than absolute oxygen vacancy density.

4. Biological application

4.1. Antioxidant activity

In this work, we evaluated the antioxidant capacity of our materials by conducting DPPH antioxidant assays. The colour of DPPH is purple, and it absorbs in the UV and visible regions at 330 and 577 nm, respectively. The peak in the UV region corresponding to $\pi \rightarrow \pi^*$ electronic transitions (responsible for the nitrogen center radical), and the peak at 577 nm, in the visible region, gives the deep violet colour of the stable free radical; this peak is particularly important for antioxidant studies, as it reflects the presence of unpaired electrons in DPPH.[42]

When the NPs interact with DPPH, the scavenging of free radicals can occur in different ways, such as direct electron transfer (ET), hydrogen atom transfer (HAT), and surface-mediated redox cycling. Fig. 9 exhibits the UV-visible spectra

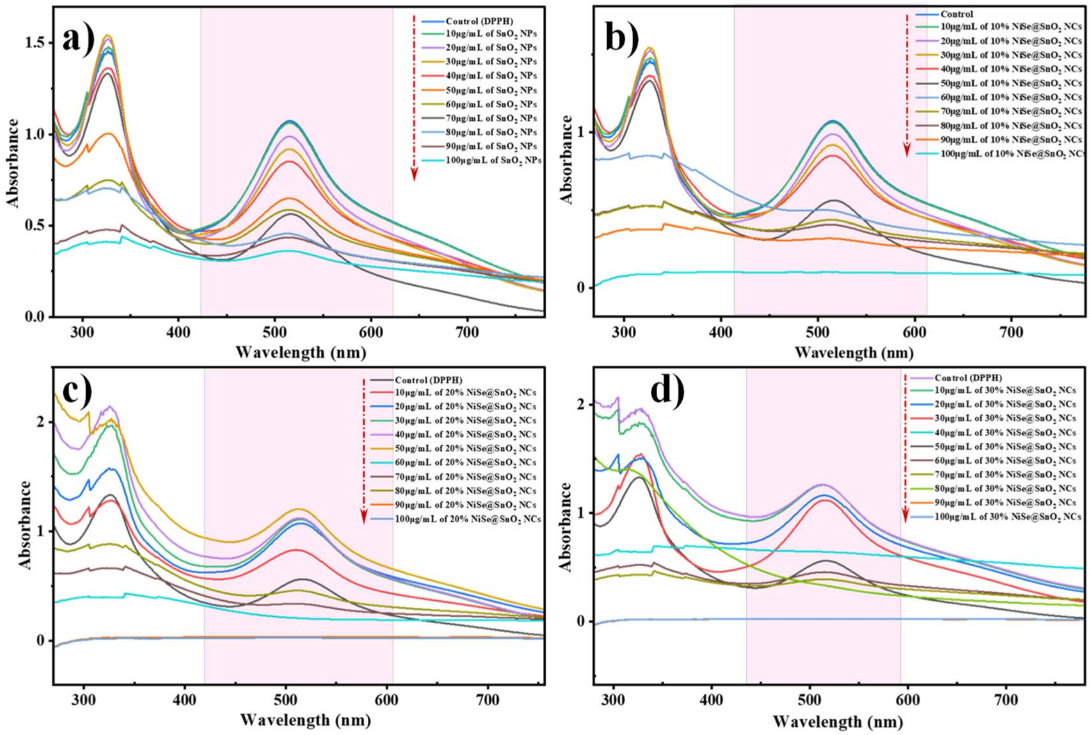

Fig. 9 (a–d) UV-visible spectra of the undoped SnO_2 NPs and 10, 20 and 30% $NiSe_2$-doped SnO_2 NCs at different concentrations (10–100 µg mL^{-1}) treated with DPPH.

of DPPH with different concentrations of undoped SnO_2 NPs and $NiSe_2$-doped SnO_2 NCs. When the concentration of the NPs increases (10 to 100 µg mL^{-1}), the 577 nm peak intensity decreases; at higher concentrations of our material, the intensity drops to near zero compared to untreated DPPH.

The main reason for the decrease in peak intensity was due to the reduction of DPPH radicals as well as intramolecular charge transfer (ICT) processes induced by the NPs. The NPs can donate electrons (ET) or hydrogen atoms (HAT) to DPPH, facilitating electron delocalization within the DPPH molecule and altering its electronic structure. This ICT effect destabilizes the radical's conjugated system; the incoming electron redistributes electron density across the conjugated π-system. This redistribution destabilizes the radical's delocalized electronic structure, altering the energy levels of the molecular orbitals involved in the electronic transition responsible for absorption at 517 nm. As a result, the probability of the $\pi \rightarrow \pi^*$ transition decreases, leading to a reduction in absorbance at 517 nm. At higher NP concentrations, more electrons are transferred to neutralize the free radical and enhance ICT, which can cause the peak to diminish to near zero. Thus, the observed decrease in the 517 nm peak reflects a combination of direct radical scavenging and ICT-induced disruption of the radical's conjugation.

An additional peak appears around 330 nm is observed, this peaks corresponds to $\pi \rightarrow \pi^*$ transition of benzenoid aromatic ring. This benzenoid aromatic ring is not directly involved in radical scavenging. When ET occurs in the DPPH molecule, the electronic density is altered in the conjugated system. This can enhance shift level of $\pi \rightarrow \pi^*$ transition, causing either increases and decreases, depending on electron delocalization. In our case, when the NPs were incorporated at lower concentrations, the peak intensity increased, whereas at higher concentrations, the peak intensity decreased, similar to the visible region peak. The initial increase at low NP concentrations can be attributed to partial electron donation and intramolecular charge transfer (ICT), which slightly enhances the $\pi \rightarrow \pi^*$ transition by increasing electron density in certain regions of the conjugated system. Essentially, the molecule adjusts its electron distribution to accommodate the incoming electron, which can temporarily increase the probability of the UV transition. At higher $NiSe_2$ NP concentrations doped in the SnO_2 NCs, however, the large number of electrons donated leads to over-saturation of the π-system and destabilization of the conjugated structure, causing the $\pi \rightarrow \pi^*$ transition to become less favourable and decreasing the UV peak intensity. Additionally, at high concentrations, light scattering or aggregation effects of the NPs may also contribute to the apparent drop in intensity. Thus, the observed pattern reveals a concentration dependent balance between the over reduction of the DPPH conjugated system and ICT induced enhancement. As the concentration increases, the peaks in both the UV and visible regions diminish, indicating that the NC has strong antioxidant activity, as shown in Fig. 9a–d. In contrast, with increased dopant concentrations, much lower IC_{50} values were exhibited, suggesting improved activity based on the IC_{50} values, compared to previous literature (Table 3).

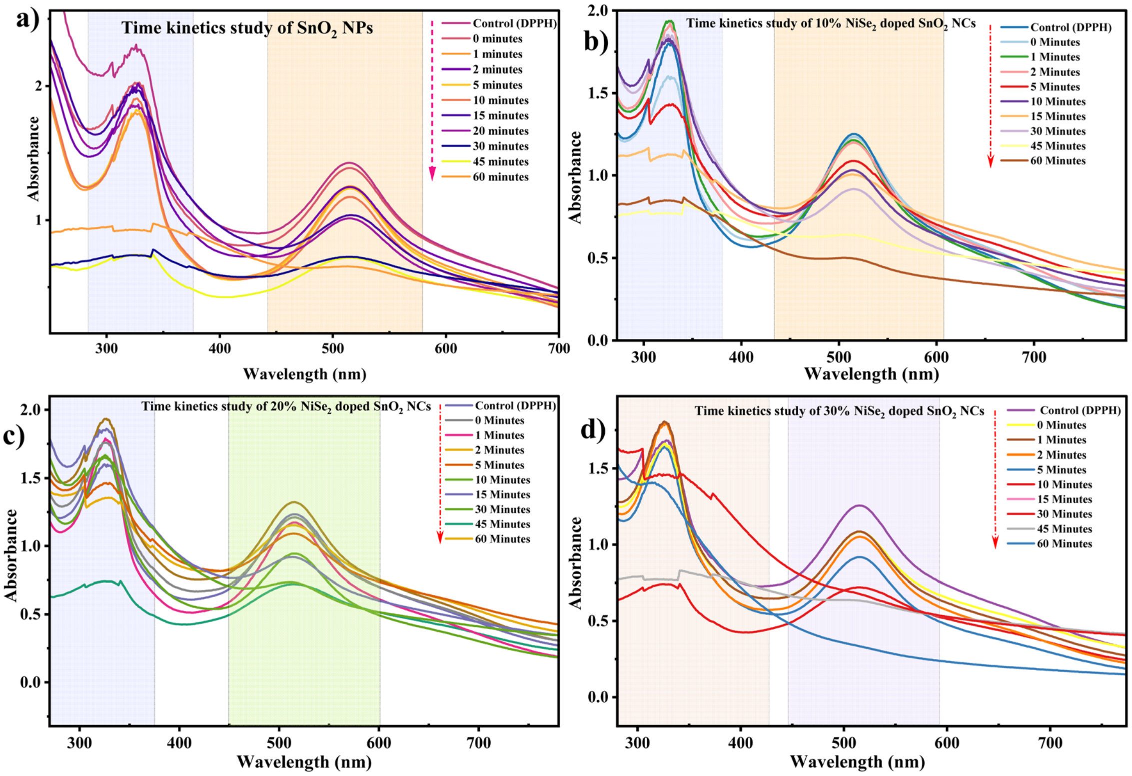

Fig. 10 (a–d) Time kinetics study of SnO_2 and $NiSe_2$-doped SnO_2 at different concentrations (10%, 20% and 30%) [time interval 0–60 minutes].

Table 2 Reaction kinetics, rate constant, half-life and IC_{50} value of the undoped SnO_2 NPs and $NiSe_2$-doped SnO_2 NCs at different concentrations (10%, 20%, and 30%)

Sample	Order of the kinetics	*K* (rate constant)	$t_{1/2}$ (min^{-1})	IC_{50} (μg mL^{-1})	Observation
Undoped SnO_2 NPs (T)	Second order	0.01949 ± 0.00180.01949	6.5771.1 ± 6.57	72	Slow reaction and higher IC_{50} value
10% $NiSe_2$-doped SnO_2 NCs (M)	Zero order	0.00956 ± 5.88 × 10^{-4}	64.5 ± 4.0	54	Moderate reaction
20% $NiSe_2$-doped SnO_2 NCs (N)	Second order	0.01257 ± 9.91 × 10^{-4}	97.9 ± 7.72	48.5	Slow kinetics ($t_{1/2}$ is higher) but better IC_{50}
30% $NiSe_2$-doped SnO_2 NCs (O)	First order	0.01806 ± 0.00212	38.15 ± 4.45	41.2	Faster (shorter $t_{1/2}$, higher *k*), best antioxidant

Fig. 10a–d shows the UV-visible spectra obtained in the kinetic studies. The DPPH absorption peaks decrease gradually over a period of 0 to 60 minutes. After 60 minutes, the distinctive bands dropped to virtually baseline levels, when the NCs donate electrons or hydrogen atoms to DPPH to scavenge the free radicals. This indicates that the radicals had been completely scavenged. As a result, at higher concentration of the $NiSe_2$-doped SnO_2 NCs both the UV (~330 nm) and visible (~517–577 nm) peaks disappear completely within 60 minutes.

Both the rate constant (*k*) and the half-life ($t_{1/2}$) are important parameters in chemical kinetics; the rate constant is used to determine reaction speed, and the half-life is used to determine the time required for the reactant concentration to drop to half of its original value. The relationship between *k* and $t_{1/2}$ changes depending on the order of the reaction. In first-order reactions, the half-life is unrelated to initial concentration. In zero-order reactions, it decreases linearly with respect to the initial concentration, and it is inversely related to the rate and initial concentration in second-order reactions. Collectively, these characteristics provide important insights into the molecular pathways and comparative systems.

By applying the experimental data to the integrated rate equation that corresponds to the order of the reaction. We found the best fit by considering the linearity (r^2) of the plots of $[A]$ *vs.* t (zero-order), $\ln[A]$ *vs.* t (first-order), and $1/[A]$ *vs.* t (second-order). The reaction order was selected as the model with the best correction coefficient.[43,44]

Table 2 shows that sample T followed second-order kinetics, indicating moderate reaction speed, with a rate constant of 0.01949 ± 0.00180.01949 and a half-life of 6.5771 ± 6.57

Table 3 30% $NiSe_2$-doped SnO_2 NCs: comparison with literature and key mechanisms

Antioxidant	Synthesis method	Antioxidant assay	Key mechanism	IC_{50} value	References
SnO_2 NPs	Microemulsion method	DPHH assay	Limited surface-active sites and poor electron-donating ability due to large band gap and low defect density	1.5 mg mL^{-1}	45
SnO_2	Pomegranate seeds		Surface-bound polyphenols and flavonoids facilitate electron donation to DPPH radicals	200 μg mL^{-1}	46
g-C_3N_4–g-Ag-doped SnO_2 (6 mL) QDs	Chemical synthesis		Heterojunction formation and Ag-induced charge separation electron transfer efficiency	150 μg mL^{-1}	47
SnO_2 and Al_2O_3 NPs	Chemical synthesis		Dilute active SnO_2 site and absence of redox active centre result in weak antioxidant properties	751.66 μg mL^{-1} and 894.90 μg mL^{-1}	48
SnO_2 and $Sn_{0.93}Mn_{0.07}O_2$	Green synthesis *Annona muricata*		Mn-induced lattice distortion generates defect sites that assist electron transfer	206.278 μg mL^{-1} and 381.892 μg mL^{-1}	49
SnO_2 and $Sn_{0.93}Co_{0.07}O_2$	Green synthesis *A. muricata*		Limited electron transfer from the redox active centre Co^{2+}/Co^{3+} to DPPH radicals	206.278 and 413.461 μg mL^{-1}	50
SnO_2 quantum dots	Green synthesis *Parkia speciosa*		Quantum confinement and increases in the surface-volume ratio enhance radical adsorption	312.6 μg mL^{-1}	51
Phyto-SnO_2 and 30% CuSe doped SnO_2 NCs	Green synthesis *Justicia adhatoda*		Synergistic effect of phytochemical functionalization and CuSe–SnO_2 interfacial charge transfer enhances electron donation	99.58 μg mL^{-1} and 56.49 μg mL^{-1}	52
Undoped SnO_2 NPs and 30% $NiSe_2$-doped SnO_2 NCs	Green synthesis *Justicia adhatoda*		Oxygen-vacancy-rich defect states act as the primary active site for the radical adsorption and electron donation, while $NiSe_2$-induced heterojunction formation facilitates charge transfer, and stabilizes vacancy-associated electron transfer for efficient DPPH radical scavenging	72 μg mL^{-1} and 41.2 μg mL^{-1}	This work

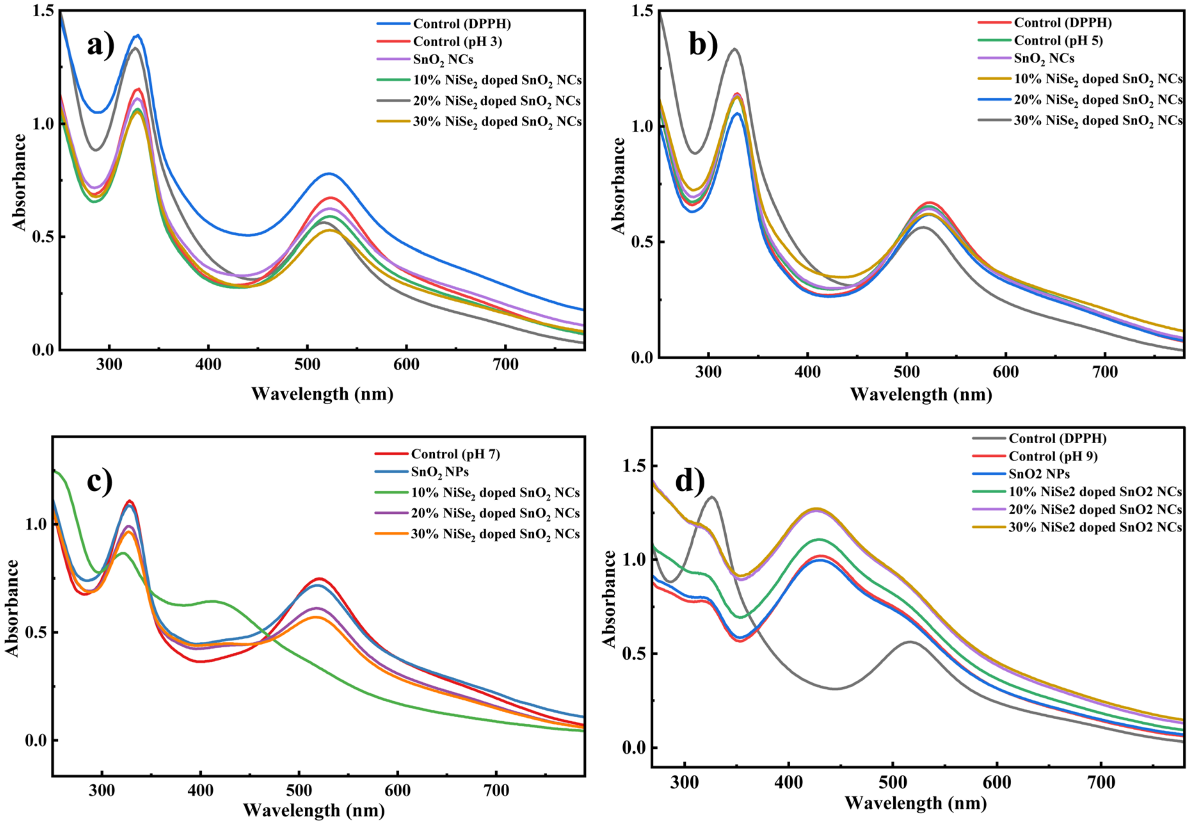

Fig. 11 (a–d) UV-visible spectra of the undoped SnO$_2$ NPs and 10, 20, and 30% NiSe$_2$-doped SnO$_2$ NCs treated with DPPH at different pH (3, 5, 7, and 9).

minutes. Sample M was best described by the zero-order model and had a rate constant of $-0.00956 \pm 5.88 \times 10^{-4}$ and a half-life of -64.5 ± 4.0 minutes, suggesting a constant rate process that is unrelated to the concentration of reactant. Sample N was related to Sample T, was also second-order, but it had slower reaction kinetics with a longer half-life of 97.9 ± 7.72 minutes and a lower rate constant of $0.01257 \pm 9.91 \times 10^{-4}$. Sample O was best described by the first-order model, with a faster reaction rate compared to the other samples, with a rate constant of -0.01806 ± 0.00212 and a half-life of 38.15 ± 4.45 minutes; its shorter half-life indicates more rapid reaction kinetics. Samples with shorter half-lives and higher rate constants showed lower IC$_{50}$ values, indicating enhanced scavenging activity, as shown in Fig. S4.

Fig. 11a–d shows that the intensities of the UV and visible region peaks for DPPH decrease at pH 3 and pH 5 without any noticeable position changes, indicating that there was no structural disruption in the mildly acidic environment. Only Sample M incorporated DPPH; as we can see, the peak shifts toward lower wavelengths at pH 7, whereas other concentrations showed no change. This suggests that a slight lattice expansion occurred due to the limited incorporation of hydroxyl ions at neutral pH. We can see a notable change at pH 9, due to lattice expansion, increased oxygen site deprotonation, and surface hydroxylation. Additionally, a higher pH enhances ionic interactions with the dopant, resulting in changes to the crystallographic parameters. The results indicate that the lattice parameters and structural integrity of the NCs are sensitive to the pH of their surroundings, with the impact being more noticeable in basic environments.

The control DPPH ESR spectrum showed a clear triplet pattern with a strong signal in the magnetic field range of 3480–3540 G. When the unpaired electron of the DPPH radical interacts with a magnetic moment of nitrogen nucleus ($I = 1$), hyperfine splitting results in this triplet. Three possible spin states (+1, 0, and −1) are present in the nitrogen nucleus, and the unpaired electron interacts with each of these states to generate three lines that are equally spaced and have comparable intensities. In comparison to the control, the ESR signal intensity of DPPH for samples T, M, and N gradually decreased after treatment of the NCs. This implies that the NCs can effectively scavenge radicals by transferring electrons or hydrogen atoms. In contrast to the other samples, sample O caused complete decrease of the DPPH signal to baseline, indicating significantly higher antioxidant activity.

Fig. 12a shows the FTIR spectra of the treated nanoparticle samples (T, M, N, and O) and the control DPPH, showing significant changes in the band locations and intensities. The results are consistent with ESR results and suggest interactions between the NCs and DPPH radical. The sequence of C > O > T > M > N was observed in the extensive OH stretching vibration (3318 cm^{-1}), indicating a decrease in hydroxyl-related

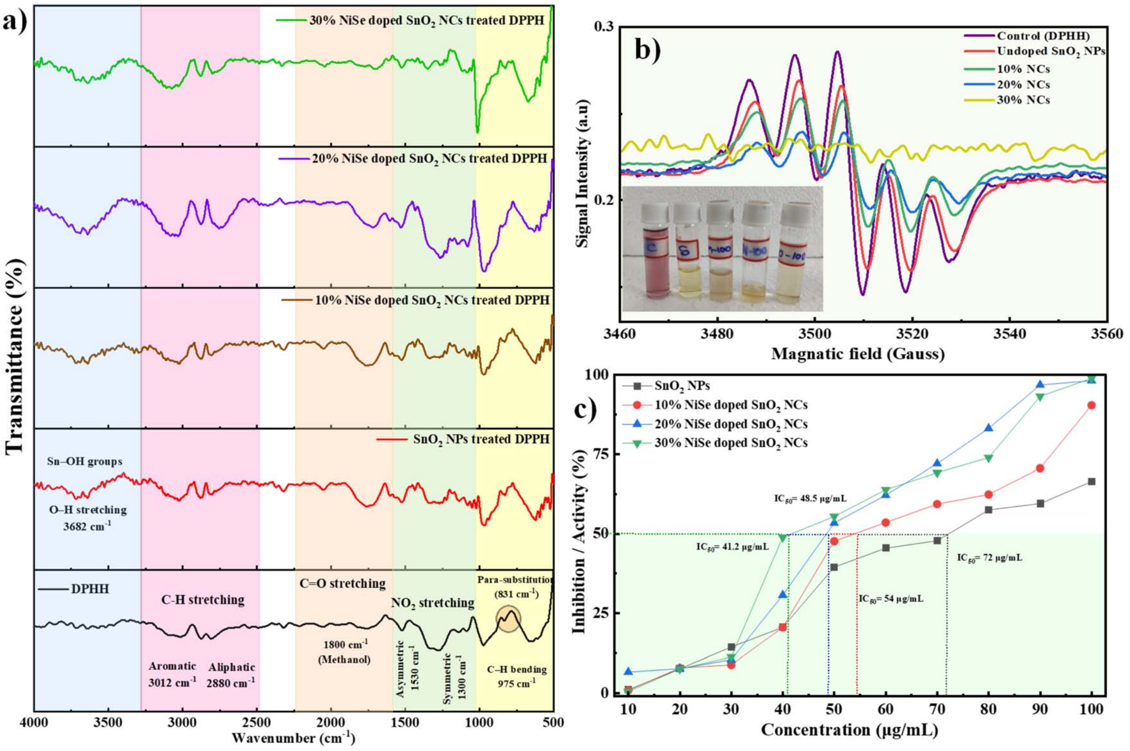

Fig. 12 (a–c) FTIR spectra, ESR spectra with inset photographs, and IC_{50} values of DPPH-treated SnO_2 NPs and $NiSe_2$-doped SnO_2 NCs at different doping concentration (10%, 20% and 30%).

vibrations caused by hydrogen atom transfer (HAT), which corresponds to antioxidant activity. The C–H stretching bands (2944–2832 cm^{-1}) exhibited two patterns O > C > T > M > N and O > T > C > N > M, suggesting that higher $NiSe_2$ doping, particularly in O, enhances C–H bond perturbation, reflecting structural reorganization during DPPH reduction. The aromatic C═C stretching (1633 cm^{-1}) exhibited the sequence N > M > O > C > T, showing enhanced preservation of aromatic conjugation in N and M, while T and O demonstrated increased disruption due to more potential to donate electrons. Asymmetric and symmetric nitro (–NO_2) stretching (~1456–1412 cm^{-1}) followed O > C > T > N > M, demonstrating that the O sample (30% $NiSe_2$ doping) most effectively perturbs the nitro functional group, consistent with near-complete DPPH reduction observed in ESR, shown in Fig. 12b and c. Bands corresponding to C–H vibrations within the nitrogen framework (2524–2231 cm^{-1}) were more intense in O > C > M > T > N, supporting the superior radical quenching ability of sample O. The C–H bending (~1019–679 cm^{-1}) decreased in the order O > C > T > N > M, indicating stronger distortion of the aromatic ring hydrogens, while phenyl ring substitution vibrations followed O > C > M > N > T, confirming that sample O most significantly modifies the aromatic environment of DPPH.

In particular, in the O sample (30% $NiSe_2$-doped SnO_2 NCs), all characteristic FTIR bands of DPPH decreased in intensity when compared with the control, including O–H (~3318 cm^{-1}), C–H stretches (2944–2832 cm^{-1}), aromatic C═C (~1663 cm^{-1}), nitro asymmetric/symmetric stretches (~1456–1412 cm^{-1}), the coupled C–N/N–N region (~1020 cm^{-1}), and the out-of-plane C–H/phenyl substitution band (~680 cm^{-1}). The global attenuation of these vibrations indicates a near-complete neutralization of the DPPH radical by sample O, consistent with the complete disappearance of the DPPH ESR signal for this sample. Mechanistically, the uniform decrease across the spectral fingerprint suggests that electron transfer and/or hydrogen-atom transfer from the nanoclusters effectively delocalize and stabilize the radical center, perturbing the entire aromatic and nitro hydrazyl framework without cleaving the molecular backbone. The absence of new FTIR bands or major shifts further supports a non-destructive reduction to DPPH–H rather than chemical degradation.

Overall, the combined FTIR and ESR results demonstrate that nanoparticle treatment progressively scavenged free radicals. The OH, CH, nitro and phenyl substitution bands showed the greatest disruption in sample O, which is consistent with their increased radical scavenging capability. Essential aromatic and nitro vibration are still present, indicating that the NP's primary work is to donate the electron to form $DPPH^-$ and its protonated form in aqueous solution, while preserving the molecular structure.

4.1.1 DPPH radical scavenging mechanism: a multifaceted approach. The antioxidant activity of $NiSe_2$-doped SnO_2 NCs can be elucidated through three synergistic pathways, all affected by oxygen vacancies (V_O) and interfacial charge-transfer processes. The unique mechanism is correlated to the XPS results (pre- and post-reaction).

4.1.1.1 Pathway 1: the principal routes involve direct electron transfer from oxygen vacancies

4.1.1.1.1 Step: 1 transfer of electron and adsorption. As it approaches the surface of the NPs, a DPPH$^•$ radical is adsorbed straight onto an V_O site. The two localized electrons at the V_O sites are readily transferred to the DPPH$^•$ radical, and the V_O serves as an electron-rich center that stabilizes the radical species, as represented in eqn (7):

$$V_o\ (2e^-) + DPPH^• \rightarrow V_O{+} + DPPH^- \quad (8)$$

This reaction converts the DPPH$^•$ into a stable anionic intermediate (DPPH$^-$).

4.1.1.1.2 Step: 2 anionic intermediates neutralized by protons unique mechanism is correlated. A non-radical compound is formed when the DPPH$^-$ anion rapidly accepts a proton (H$^+$) from the surrounding medium or from surface –OH groups of NPs, as shown in eqn (8)

$$DPPH^- + H^+ \rightarrow DPPH\text{–}H \quad (9)$$

4.1.1.1.3 XPS correlation. The electron-donation event alters the chemical environment of the V_O sites, allowing for the adsorption of oxygenated species such as O^{-II} or ^-OH to stabilize the electron-deficient vacancies. This change increases the relative strength of the V_O component in the O 1s spectrum, corresponding to the near 8-fold increases observed in experimental results.

4.1.1.2 Pathway 2: electron transfer through $NiSe_2$-doped SnO_2 nanocomposites as a heterojunction. As an electron reservoir, $NiSe_2$ continuously transports electrons into the SnO_2 conduction band V_O states over the heterojunction interface. The scavenging cycle is maintained by the electrons being easily transferred to adsorbed DPPH$^•$ radicals, as shown in eqn (9):

$$NiSe_2 \rightarrow SnO_2\ (V_O) \rightarrow DPPH^• \rightarrow DPPH\text{–}H \quad (10)$$

By restoring the electron density at the V_O sites, the dynamic electron mobility improves the composite system efficiency and adds to its partially self-regenerative radical scavenging capabilities.

4.1.1.3 Pathway 3: hydrogen/radical abstraction through surface hydroxyl groups (secondary route). Scavenging hydrogen directly from surface –OH groups is an example of a parallel process, as shown in eqn (10).

$$\text{Surface-OH} + DPPH^• \rightarrow \text{Surface-O}^• + DPPH\text{–}H \quad (11)$$

The neighbouring lattice stabilizes the resulting surface oxygen radical (surface-O$^•$), or it may recombine with another radical species.

4.1.1.3.1 XPS correlation. The noted decrease in the intensity of the –OH component in the O 1s XPS spectrum after DPPH exposure corroborates this process by confirming that surface hydroxyl groups are partially reduced, as shown in Fig. 6b, due to radical neutralization.

4.1.1.3.2 Overall mechanistic insights. The significant antioxidant activity and the alterations observed in the post-reaction XPS of the $NiSe_2$-doped SnO_2 NCs are explained by the combined effects of (i) electron transfer made possible by oxygen vacancies, (ii) electron replenishment *via* heterojunctions with $NiSe_2$ and (iii) the participation of surface hydroxyl groups to form DPPH–H (Fig. 13).

4.2. Antibacterial activity

The disc diffusion method was employed to evaluate the *in vitro* antibacterial efficacy of undoped SnO_2 NPs and $NiSe_2$-doped SnO_2 NCs. This work used Gram-negative bacteria *K. pneumonia* (MTCC 618), *E. coli* (MTCC 443) and *P. aeruginosa* (MTCC 1688), and the Gram-positive bacterium *S. aureus* (MTCC 96). The SnO_2 and $NiSe_2$ NPs both contributed significantly, which elucidated their efficient bactericidal characteristics. The overall efficiency was enhanced by increased $NiSe_2$ concentration at 10, 20 and 30%, compared to undoped SnO_2 NPs. The multiple antibacterial mechanistic processes of $NiSe_2$-doped SnO_2 NCs are given below.

First and foremost, mechanisms based on charge and size are more crucial. Due to their smaller, the nanoparticles can readily penetrate bacterial cell walls. In this study, Sn^{+IV} and Ni^{+II} cationic species can easily pass through the outer membrane lipopolysaccharides (LPS) and accumulate within

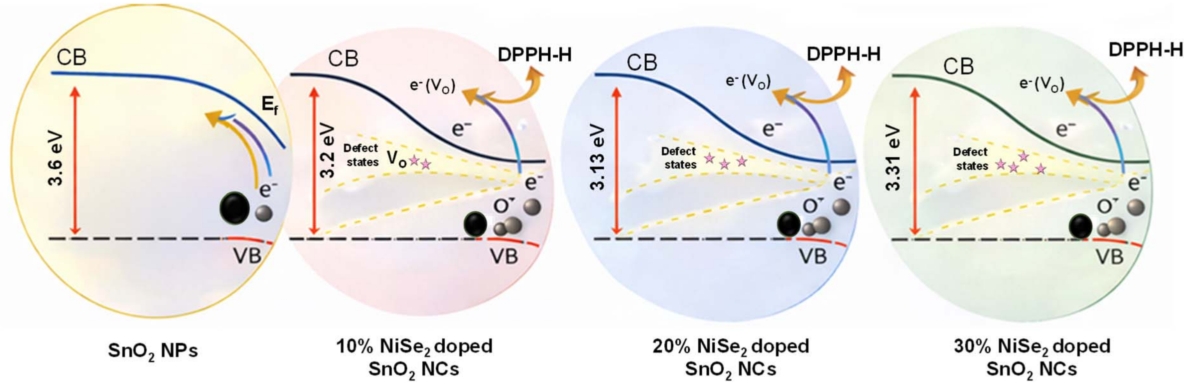

Fig. 13 Band bending diagram of the undoped SnO_2 NPs and $NiSe_2$-doped SnO_2 NCs (10%, 20% and 30%): charge-transfer mechanism for antioxidant activity.

the inner membrane. LPS have electron-donor sites, oxygen-based donors such as phosphate, carboxyl, and hydroxyl groups, that interact with metal ions to form strained complexes (metal–lipid complexes), as shown in eqn (11). It form stronger ionic connection, although weaker than covalent bond. This complex increases membrane permeability, leading to cell death by disrupting the bacterial membrane.[53]

$$[\mathrm{LPS}-\mathrm{OPO3}]\frac{\mathrm{Mg}^{+\mathrm{II}}}{\mathrm{Ca}^{+\mathrm{II}}}[\mathrm{OPO3}-\mathrm{LPS}]\rightarrow[\mathrm{LPS}-\mathrm{OPO3}]-\mathrm{M}^{+n}+\frac{\mathrm{Mg}^{+\mathrm{II}}}{\mathrm{Ca}^{+\mathrm{II}}}(\mathrm{released}) \tag{12}$$

Secondly, it is crucial to consider interactions with thiol groups. The interaction between adsorbed $\mathrm{Sn}^{+\mathrm{IV}}$ and $\mathrm{Ni}^{+\mathrm{II}}$ ions and the thiol (–SH) group of cysteine residues in bacterial enzymes can lead to the formation of new Sn–H and Ni–H bonds through hydrogen replacement, as shown in eqn (12)–(14). As a further advantage, thiol groups or ROS generated by $\mathrm{Se}^{-\mathrm{II}}$ and $\mathrm{O}^{-\mathrm{II}}$ anions on the NP's surface might induce oxidative stress. These changes make it harder for proteins to carry out important cellular tasks and enzyme activity. Blocking the enzyme β-lactamase restores bacterial susceptibility to β-lactam antibiotics, which is essential for the survival of *E. coli* and *S. aureus* under antibiotic exposure. The nitrate reductase is essential for anaerobic respiration in *P. aeruginosa*, and metal ions can render this enzyme inactive. This puts the bacteria's viability at risk and eventually causes cell death.[54]

$$\text{Cys–SH (enzyme)} + \mathrm{Sn}^{+\mathrm{IV}} \rightarrow \text{Cys–Sn} + \mathrm{H}^{+} \tag{13}$$

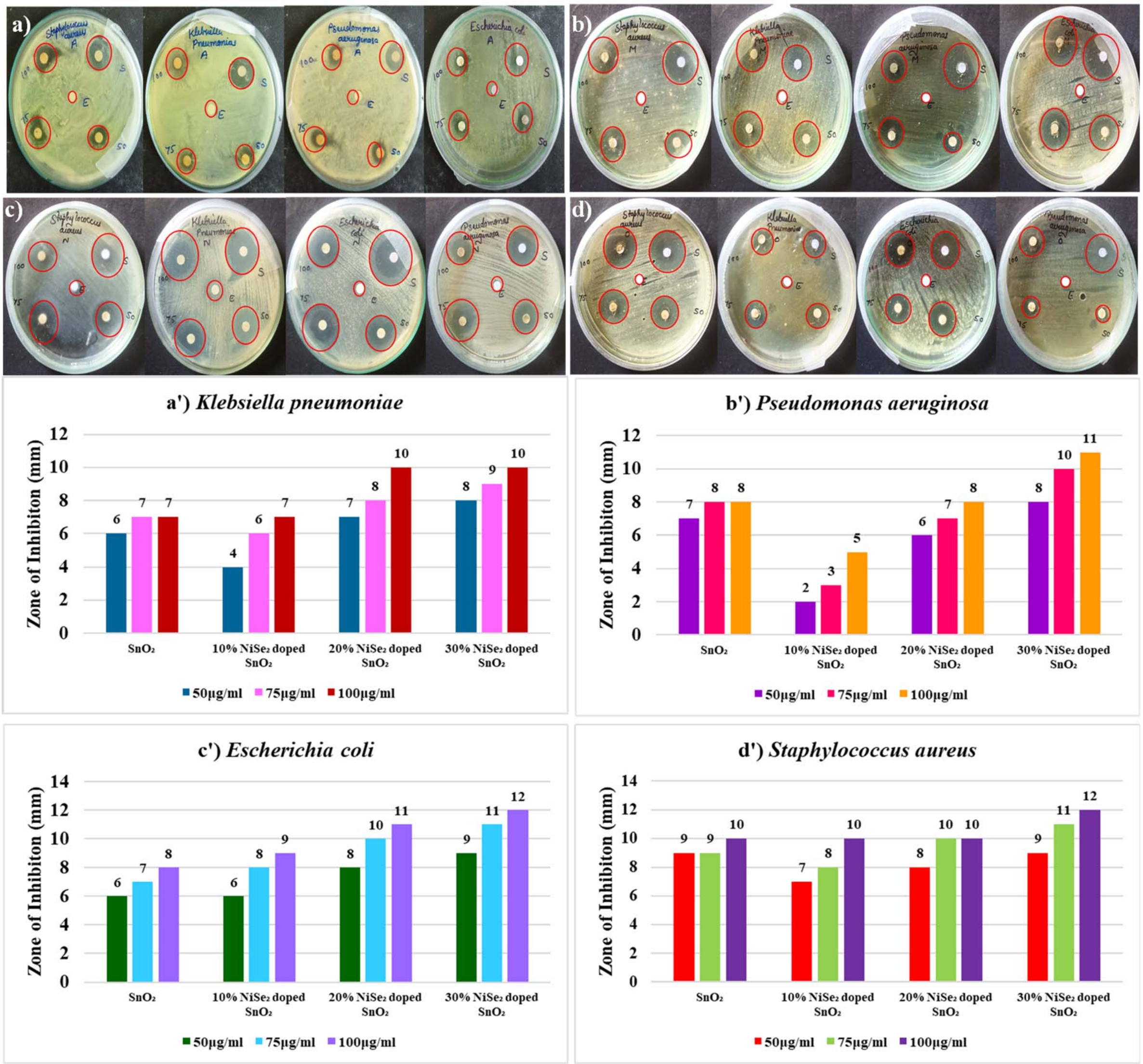

Fig. 14 (a–d) Zone of inhibition images and (a′–d′) quantitative comparison of the ZOI values for Gram-negative (*K. pneumonia*, *P. aeruginosa*, and *E. coli*) and Gram-positive (*S. aureus*) bacteria.

$$\text{Cys–SH (enzyme)} + \text{Ni}^{+\text{II}} \rightarrow \text{Cys–Ni} + \text{H}^{+} \quad (14)$$

$$\text{Cys–SH (enzyme)} + \text{Se}^{-\text{II}} \rightarrow \text{Cys–Se (thiol modification)} \quad (15)$$

Thirdly, based on the shape, bacterial membranes could sustain physical harm from NPs with sharp edges or one- or two-dimensional shapes. The mechanical consequences include lipid extraction, bubble-mediated disruption, membrane cutting and instability. Previous literature reports show that *E. coli* cell walls can be ruptured by forces as small as about 20 N. As such, sharp-edged nanomaterials could function like a knife, efficiently breaking and disrupting the membrane.[55]

The reactive oxygen species (ROS) production as the concentration dependent process.[30] The NPs exhibit enhanced antibacterial activity with increasing dopant ($NiSe_2$) concentration in the composite. Lower concentrations are insufficient to produce ROS to inhibit or kill the bacteria. Superoxide dismutase (SOD), which efficiently neutralizes superoxide anions, is produced by bacteria in response to small quantities of ROS. Overproduction of ROS damages proteins, lipids, and DNA, ultimately leading to bacterial death. Fig. 14a–d shows the antibacterial activity ranked as O > N > M > T, indicating that sample O had superior activity against *K. pneumonia*, *P. aeruginosa*, *S. aureus* and *E. coli*.

The characterization results provide further evidence for the superior antibacterial efficiency of sample O. The XRD results showed that sample O had the largest peak shift and lattice strain, which makes the surface of the NCs more reactive. The FTIR spectra confirm that the obtained functional groups reduce free radicals, while the UV-visible investigations demonstrate the improved catalytic effectiveness. XPS and ESR investigations performed before and after DPPH contact indicate that sample O generates ROS with increasing concentration and maintains advantageous oxidation states ($Sn^{+IV}/Se^{-II}/Ni^{+II}$), thereby promoting redox cycling at the bacterial interface. These results show that sample O is the best antibacterial agent among the synthesised materials, because of its structural change and better redox activity.

5. Conclusion

This work describes the effective synthesis of $NiSe_2$-doped SnO_2 NCs using *Justicia adhatoda* leaf extracts at different concentrations 10%, 20% and 30%. The crystal nature was confirmed by structural analysis, and the peak shift indicates that $NiSe_2$ was effectively doped into the SnO_2 crystal lattice, while secondary peaks support the formation of NCs. Due to doping effects, UV-visible spectroscopy revealed notably decreased (at lower concentration doping) and increased (at higher concentration doping) band gaps. While EDX and XPS investigation verified the chemical composition and oxidation states, TEM and SEM analyses revealed the irregular spherical and cluster-shaped morphology of the NPs and NCs, respectively.

By optimizing the pH and NC concentration, the DPPH assay was used to determine antioxidant activity. Although pH 3, 5, and 7 showed minimal influence on scavenging activity, the DPPH analysis at pH 9 exhibited an irregular peak. The IC_{50} value for the 30% $NiSe_2$-doped SnO_2 NCs was 41.2 μg mL^{-1}, whereas the IC_{50} of SnO_2 NPs was 77 μg mL^{-1}. The FTIR spectrum shows the appearance of a new OH stretching band with no other significant peak changes, while the ESR spectrum lacks the characteristic triplet signal, indicating complete scavenging of radicals by the NCs.

According to post-reaction characterizations conducted after DPPH inclusion, the XRD peaks showed a noticeable shift towards higher angles at higher doping concentrations but very slight structural changes at lower concentrations. Post SEM analysis confirmed particles agglomeration, indicating direct surface contact between the particles. Post XPS results showed no significant changes in the metals and Se chemical states; however, the O 1s peak showed variation in the oxygen vacancies deconvolution peak. Furthermore, zeta potential analysis confirmed an oxygen vacancy mediated radical scavenging process. Significant antibacterial activity against *Klebsiella pneumoniae* (10 mm), *Pseudomonas aeruginosa* (11 mm), *Escherichia coli* (12 mm), and *Staphylococcus aureus* (12 mm) was demonstrated by the 30% $NiSe_2$-doped SnO_2 NCs (Sample O), highlighting its potential for environmentally friendly biomedical applications.

Author contributions

Mohamed Ashik Syra: conceptualization, methodology, investigation, software, validation, formal analysis and writing – original draft. Sangeetha Alaguvel: writing, review, editing, software and data curation. Devikala Sundaramurthy: conceptualization, resources, formal analysis, visualization and supervision.

Conflicts of interest

The authors declare that there are no known competing financial interests or personal relationships that could have appeared to influence the work.

Abbrevations

NPs	Nanoparticles
NCs	Nanocomposites
SnO_2	Tin Oxide
$NiSe_2$	Nickel Selenide
XRD	Powder X-ray Diffraction
UV	UV-visible spectroscopy
HRSEM	High-Resolution Scanning Electron Microscopy
EDX	Energy-Dispersive X-ray Analysis
FTIR	Fourier Transform Infrared Spectroscopy
TEM	Transmission Electron Microscopy
ESR	Electron Spin Resonance Spectroscopy
DDW	Double-Distilled Water
JCPDS	Joint Committee on Powder Diffraction Standards
nm	Nanometres
SAED	Selected Area Electron Diffraction
XPS	X-ray Photoelectron Spectroscopy
DPPH	2,2-Diphenyl-1-Picrylhydrazyl

ROS	Reactive Oxygen Species
IC_{50}	Half-maximal inhibitory concentration

Data availability

The data supporting the findings of this study are available from the corresponding author upon reasonable request.

Supplementary information (SI): materials, instrumentation, analytical procedures, XRD Rietveld refinement spectra of SnO_2 and $NiSe_2$ NPs, the particle size distribution of SnO_2 and $NiSe_2$ NPs, pre- and post-reaction XPS characterization of 30% $NiSe_2$-doped SnO_2 NCs, and rate kinetics of SnO_2 and $NiSe_2$-doped SnO_2 NCs at different concentrations (10%, 20% and 30%). See DOI: https://doi.org/10.1039/d6ra00150e.

Acknowledgements

The authors would like to thank Central Instrumentation Facility (CIF), IIT Jammu and IIT Bombay (SAIF) for providing instrumental and analytical support. The author also thank to Nanotechnology Research Centre (NRC), SRM-IST, for providing the research facilities.

References

1 İ. Gulcin, Antioxidants and antioxidant methods: an updated overview, *Arch. Toxicol.*, 2020, **94**(3), 651–715.
2 M. E. Büyükokuroğlu, I. Gülçin, M. Oktay and O. I. Küfrevioğlu, *Pharmacol. Res.*, 2001, **44**, 491–494.
3 M. Musialik, R. Kuzmicz, T. S. Pawłowski and G. Litwinienko, *J. Org. Chem.*, 2009, **74**, 2699–2709.
4 I. G. Munteanu and C. Apetrei, *Int. J. Mol. Sci.*, 2021, **22**, 3380.
5 C. Yang, Y. Lu, L. Zhang, Z. Kong, T. Yang, L. Tao, Y. Zou and S. Wang, *Small Struct.*, 2021, **2**, 2100058.
6 A. Galano and M. Francisco-Marquez, *J. Phys. Chem. B*, 2009, **113**, 11338–11345.
7 Z. Huang, J. Zhu, Y. Hu, Y. Zhu, G. Zhu, L. Hu and Y. Zi, *Nanomaterials*, 2022, **12**, 632.
8 S. Suthakaran, S. Dhanapandian, N. Krishnakumar and N. Ponpandian, *J. Phys. Chem. Solids*, 2020, **141**, 109407.
9 S. K. Jain, M. Fazil, F. Naaz and A. Pandit, *New J. Chem.*, 2022, 2846–2857.
10 L. V. Antisari and S. Carbone, *Environ. Sci. Pollut. Res.*, 2015, **22**, 1841–1853.
11 L. Ali, S. Ali, N. Ali, L. Zhu and S. Zulfiqar, *Ceram. Int.*, 2025, **51**, 6783–6792.
12 A. Banik, M. S. Ansari and M. Qureshi, *ACS Omega*, 2018, **3**, 14482–14493.
13 M. Pirsaheb, T. Gholami, H. Seifi, E. A. Dawi and E. Ahmed, *Environ. Sci. Pollut. Res.*, 2024, **31**, 24768–24787.
14 D. L. P. Prabu, G. G. S. Munusamy and S. S. C. Arulvasu, *SN Appl. Sci.*, 2019, **1**, 1–14.
15 N. Behera, M. Arakha and M. Priyadarshinee, *RSC Adv.*, 2019, **9**, 24888.
16 S. Sahoo, D. Chatterjee, S. B. Majumder, K. M. A. Raihan, B. LaCroix and S. R. Das, *Appl. Res.*, 2024, **3**, e202400034.
17 A. Joseph, D. Sai, H. Kumar, M. Ramadoss and K. Muralidharan, *J. Solid State Electrochem.*, 2025, **29**, 4461–4471.
18 M. Ahmad, *Inorg. Chem. Front.*, 2022, **9**(3), 448–457.
19 G. Guan, J. Wu, J. Huang and X. Qian, *J. Electroanal. Chem.*, 2022, **924**, 116888.
20 S. A. Kumar, S. Nadavurmath, S. Sahoo, G. K. Laxminarayana and C. S. Rout, *ACS Appl. Electron. Mater.*, 2025, **7**, 8850–8860.
21 J. Yang, Z. Sun, J. Wang, J. Zhang, Y. Qin, J. You and L. Xu, *CrystEngComm*, 2019, 994–1000.
22 V. S. Bhat, J. M. Shivanna, A. Shetty, V. Molahalli, S. G. Krishnan, S. Sahoo, R. K. Pai, T. M. Aminabhavi and G. Hegde, *Energy Fuels*, 2025, **39**, 16737–16767.
23 S. Sahoo, *Nanoscale Adv.*, 2025, 3331–3343.
24 S. Hariharan and S. Dharmaraj, *Inflammopharmacology*, 2020, **28**, 667–695.
25 D. Turck, T. Bohn, J. Castenmiller, S. De Henauw, H. K. Knutsen, A. Maciuk, I. Mangelsdorf, K. Pentieva, A. Siani, F. Thies, H. J. Mcardle, C. Pel, S. Tsabouri, M. Vinceti, P. Aggett, M. C. Bou, F. Cubadda, L. Fabiani, A. Titz, A. Naska and L. Ciccolallo, *EFSA J.*, 2023, **21**, e07704.
26 M. A. Syra and S. Devikala, *Inorg. Chem. Commun.*, 2024, **170**, 113373.
27 C. Gunawan, M. S. Lord, E. Lovell, R. J. Wong, M. S. Jung, D. Oscar, R. Mann and R. Amal, *ACS Omega*, 2019, **4**, 9473–9479.
28 Y. Wang, M. Zhang, S. Lv, X. Li, D. Wang and C. Song, *ACS Omega*, 2020, **5**, 13994–14005.
29 W. Yu, F. Chen and L. Zhao, *RSC Adv.*, 2020, **10**, 29082–29089.
30 V. L. Prasanna and R. Vijayaraghavan, *Langmuir*, 2015, 1–29.
31 C. Karunakaran, S. SakthiRaadha, P. Gomathisankar and P. Vinayagamoorthy, *RSC Adv.*, 2013, **3**, 16728–16738.
32 S. U. Khan, R. Hussain, Z. Ali, R. Maryam and A. Hussain, *RSC Adv.*, 2024, **14**, 28626–28637.
33 D. V Likhachev, N. Malkova and L. Poslavsky, *Thin Solid Films*, 2015, **589**, 844–851.
34 X. Lv, J. Gong, S. Wang, X. Yan, C. Sun and X. Hu, *Adv. Energy Mater.*, 2025, **15**, 1–35.
35 D. I. Khomskii and S. V. Streltsov, *Chem. Rev.*, 2021, 1–45.
36 S. Kucharski, M. Vorochta, L. Piliai, A. M. Beale and C. Blackman, *ACS Sens.*, 2025, **10**, 1898–1908.
37 V. A. Online, K. Li, Y. Peng, S. Li, F. Luo, J. Li, H. Ju, Y. Yang and Y. Li, *RSC Adv.*, 2025, **15**, 27441–27451.
38 S. Meyyanathan and D. Sundaramurthy, *J. Alloys Compd.*, 2025, **1013**, 178425.
39 S. Meyyanathan and D. Sundaramurthy, *ACS Appl. Eng. Mater.*, 2025, **3**, 3381–3402.
40 N. Özcan, T. Kortelainen, V. Golovanov, T. T. Rantala and J. Vaara, *Phys. Rev. B: Condens. Matter Mater. Phys.*, 2010, **55**, 1–10.
41 Z. Zhang, B. Yang, L. Chen, Z. Zhang and J. Guo, *Nat. Commun.*, 2025, **16**, 7015.
42 S. Baliyan, R. Mukherjee, A. Priyadarshini, A. Vibhuti, A. Gupta, R. P. Pandey and C. Chang, *Molecules*, 2022, **27**, 1326.

43 S. Mohandoss, H. Mohan, N. Balasubramaniyan and S. Loganathan, *Plasma*, 2025, 1–24.

44 H. Mohan, S. Mohandoss and N. Balasubramaniyan, *Plasma*, 2025, 1–16.

45 S. Haq, P. Ahmad, M. U. Khandaker, M. R. I. Faruque, W. Rehman, M. Waseem and S. U. Din, *Mater. Res. Express*, 2021, **8**, 035013.

46 M. Meena Kumari and D. Philip, *Powder Technol.*, 2015, **270**, 312–319.

47 M. T. Ameen, A. Haider, I. Shahzadi, A. Shahbaz, A. Ul-Hamid, H. Ullah, S. Khan and M. Ikram, *Res. Chem. Intermed.*, 2024, **50**, 1661–1678.

48 A. Giridasappa, M. I. Shareef, S. M. Gopinath, D. Rangappa, P. D. Shivaramu and C. Sabbanahalli, *Proc. Natl. Acad. Sci., India, Sect. B*, 2023, **93**, 871–882.

49 P. S. Vindhya and V. T. Kavitha, *J. Inorg. Organomet. Polym. Mater.*, 2023, **33**, 2873–2889.

50 P. S. Vindhya and V. T. Kavitha, *Biomass Convers. Biorefin.*, 2023, **14**, 25709–25726.

51 S. Begum and M. Ahmaruzzaman, *J. Photochem. Photobiol., B*, 2018, **184**, 44–53.

52 M. A. Syra and D. Sundaramurthy, *New J. Chem.*, 2025, **49**, 11032–11047.

53 H. T. Draviana, I. Fitriannisa, M. Khafid and D. I. Krisnawati, *J. Nanobiotechnol.*, 2023, **3**, 1–34.

54 Y. N. Slavin, J. Asnis, U. O. Häfeli and H. Bach, *J. Nanobiotechnol.*, 2017, 1–20.

55 S. Cha, J. Hong and M. Mcguffie, *ACS Nano*, 2015, **9**, 9097–9105.